Diagenetic characterization of crocodyliform fossils from the Adamantina Formation (Upper Cretaceous, Bauru Group): evaluating the chemical alteration of skeletal tissues through a multi-technique approach

Fellipe Muniz[1,*], Annie Hsiou[1], Fabio Dias de Andrade[2], Gabriel Osés[3], Márcia Rizzutto[3], Mirian Liza Alves Forancelli Pacheco[4]

[1]Universidade de São Paulo, Faculdade de Filosofia, Ciências e Letras de Ribeirão Preto, 14040-901, Ribeirão Preto, Brazil

[2]Universidade de São Paulo, Instituto de Geociências, 05586-010, São Paulo, Brazil

[3]Universidade de São Paulo, Instituto de Física, 05508090, São Paulo, Brazil

[4]Universidade Federal de São Carlos, Departamento de Biologia, 18052-780, Sorocaba, Brazil

*Corresponding author at: Laboratório de Paleontologia de Ribeirão Preto; Universidade de São Paulo, Ribeirão Preto, SP, Brazil.

E-mail address: fellipemuniz@yahoo.com.br (F. Muniz)

Abstract

The Adamantina Formation hosts one of the most well-documented Late Cretaceous continental faunas in South America, with crocodyliforms standing out for their unusual richness and ecomorphological diversity. While their taxonomy and anatomy have been widely studied, the understanding of their fossilization processes has been largely overlooked. Here, we apply a multi-technique approach to analyze diagenetic alterations of the skeletal elements of crocodyliforms from the Adamantina Formation, combining information from energy dispersive X-ray fluorescence, scanning electron microscopy with energy dispersive X-ray spectroscopy, micro-Raman spectroscopy, and X-ray diffraction. Our results indicate significant structural and compositional changes, including loss of the organic matrix, void permineralization, ionic substitutions, and recrystallization. Although organic molecules were not unambiguously detected, some Raman spectra exhibited bands in the 1000–1800 cm^{-1} range that resemble signals previously linked to organic compounds, but which may instead result from fluorescence induced by rare earth elements. Void-filling minerals reflect the prevailing influence of both alkaline (e.g., calcite, relict siderite) and oxidizing (iron oxyhydroxides) pore waters. All samples showed transformation of the original bioapatite into carbonated fluorapatite, highlighting the importance of the precipitation of a more thermodynamically stable phase for the long-term survival of skeletal remains. Raman spectroscopy further revealed differences in fossil apatite preservation among samples, with some showing less alteration and potentially storing original chemical information. The combination of techniques used in this study allowed a comprehensive assessment of the mode and degree of diagenetic alteration of crocodyliform remains, which might be useful when selecting samples for molecular or isotopic studies.

Keywords: Diagenesis; Fossilization; Taphonomy; Bone Preservation; Bioapatite

1. Introduction

Fresh bone and teeth consist of an association of organic (i.e., collagen, lipids) and inorganic fractions (Pfretzschner, 2004; Trueman et al., 2008; Keenan and Engel, 2017; Shah, 2025). These mineralized tissues differ structurally as the tooth enamel is harder, less porous, and contains less organic matter than dentine and bone. Dentine is more similar to bone in terms of organic content and crystal size, but is significantly less porous (Kohn and Cerling, 2002; Koch, 2007; Kendall et al., 2018). Their inorganic (i.e., mineralized) fraction is a non-stoichiometric, carbonate-bearing hydroxyapatite ($Ca_5(PO_4)_3(OH)$). The apatite lattice is particularly flexible for substitutions and can accommodate different ions at every site [calcium (Ca), phosphate (PO_4), and hydroxyl (OH)] (Pan and Fleet, 2002; Kohn, 2008). After the death of the organism, the decay of the organic matrix scaffold exposes the apatite surfaces to pore-waters, which become highly reactive due to their small crystal sizes and large surface areas (Weiner and Price, 1986; Chinsamy-Turan, 2005). During diagenesis, skeletal remains are affected by many processes, including dissolution, recrystallization, incorporation of foreign elements, and infilling of voids with authigenic or detrital minerals (Hubert et al., 1996; Trueman, 1999; Kohn and Cerling, 2002; Trueman and Tuross, 2002; Berna et al., 2004; Pfretzschner, 2004; Trueman et al. 2004, 2006, 2008; Kohn, 2008; Koenig et al., 2009; Rogers et al., 2010; Suarez et al., 2010; Kohn and Moses, 2013; Keenan, 2016; Keenan and Engel, 2017; Previtera, 2017; Rogers et al., 2020; Bosio et al., 2021; Kral et al., 2024; Laker et al., 2024; Yamamura et al., 2024). Such modifications can be informative to reconstruct past environments or preservational mechanisms but can severely overprint or erase the original chemical compositions of skeletal tissues.

The study of Cretaceous crocodyliform fossils has helped clarify several paleoecological and paleoenvironmental aspects in continental ecosystems, including the organization of trophic structures, feeding strategies, and habitat preferences (Ősi, 2014; Godoy et al., 2014; Iori and Carvalho, 2018; Melstrom and Irmis, 2019; Montefeltro et al., 2020; Nieto et al., 2022; White et al., 2022). Chemical characterizations of fossil crocodyliform bones and teeth can corroborate these studies by revealing details of the interactions between the organism and the environment, either *in vivo* (e.g., feeding habits, climate) or post-mortem (diagenesis) (Domingo et al., 2015; Marchetti et al., 2019; Alvarez et al., 2022; Klock et al., 2022). Crocodyliforms are one of the dominant components of the paleofauna from the Late Cretaceous of Brazil (Candeiro and Martinelli, 2006; Langer et al., 2022). Most occurrences are from the Adamantina Formation, where more than 20 species have been described so far. Notably, they occupied more diverse niches and displayed a higher ecomorphological diversity in relation to the living representatives of the group (Riff and Kellner, 2011; Riff et al., 2012; Godoy et al., 2014). Despite some progress made towards the understanding of major processes involved in the preservation of crocodyliforms from the Adamantina Formation, taphonomical studies are scarce and mainly focused on the biostratinomical stage (Azevedo, 2012, 2013; Araújo-Júnior and Marinho, 2013; Bandeira et al., 2018). Almost nothing is known about how diagenesis affected their skeletal remains and ultimately promoted their fossilization (Goldberg and Garcia, 2000; Marchetti et al., 2019; Pinto et al., 2020). Investigating bioapatite modification in fossils not only provides important information on diagenetic processes and burial conditions but is also key to evaluating the potential preservation of biogenic signals, whether recorded in elemental and isotopic compositions or represented by remnants of original biomolecules.

Here, we use a multi-technique approach to document the diagenetic alterations of crocodyliform specimens from the Adamantina Formation, combining data from energy dispersive X-ray fluorescence (XRF), scanning electron microscopy with energy dispersive X-ray spectroscopy (SEM-EDS), micro-Raman spectroscopy, and X-ray diffraction (XRD). We identify the main preservational mechanisms and advance understanding of the elemental and structural changes of bioapatite during fossilization.

We also discuss the implications of our diagenetic assessment of the crocodyliform fossil remains for the potential recovery of biogenic signals.

2. Material and Methods

2.1 Materials

A total of 24 fossil samples were selected from crocodyliform specimens from six different Adamantina Formation localities (see Table 1 and Fig. 1 for details). This material is housed at the Laboratório de Paleontologia de Ribeirão Preto, University of São Paulo, Brazil. The Adamantina Formation is one of the most widely distributed units of the Bauru Group, outcropping in the states of São Paulo, Minas Gerais, Goiás, and Mato Grosso do Sul (Fernandes and Coimbra, 1996; Menegazzo et al., 2016). It typically comprises reddish, fine to very fine sandstones that are massive or display cross-stratification. The sandstones are sometimes intercalated by mudstone or conglomerates (Soares et al., 1980; Batezelli, 2015; Menegazzo et al., 2016; Soares et al., 2020). The depositional setting is usually interpreted as a fluvial environment under a warm, arid to semi-arid climate (Batezelli, 2015; Basilici et al., 2016; Batezelli et al., 2019). Some lithostratigraphic proposals have suggested division of the Adamantina Formation in the state of São Paulo into smaller units, such as the Vale do Rio do Peixe, São José do Rio Preto, and Presidente Prudente formations (Fernandes and Coimbra, 2000). However, since the Adamantina Formation is widely regarded in the literature as a single unit at the formation level, we adopted this convention in our study (see discussion in Langer et al., 2022; Delcourt et al., 2024). The age of the Adamantina Formation is debated, but a Campanian–Maastrichtian age is commonly suggested based on palynology and vertebrate fauna (Langer et al., 2022; Arai and Fernandes, 2023; Gobbo and Bertini, 2023).

[insert Figure 1 here]

The analyses were performed on 12 specimens derived from the crocodyliform species *Aplestosuchus sordidus* (Godoy et al., 2014), *Aphaurosuchus escharafacies* (Darlim et al., 2021), *Pissarrachampsa sera* (Montefeltro et al., 2011), *Mariliasuchus sp.,* and other unidentified crocodyliforms. The sampled material includes teeth and different types of bones. Sampling focused on skeletal elements that were already disarticulated and/or fragmented to prevent further damage to the specimens. We also avoided samples with clear evidence of glues or other stabilizing products. Sediment samples originally associated with the fossil specimens were also analyzed whenever possible. Details about each sample are provided in Table 1.

For comparative purposes, we analyzed skull fragments and teeth from a modern caimanine alligatorid carcass, collected by a herpetologist on the banks of the Miranda River in the state of Mato Grosso do Sul, Brazil. The same analytical parameters were applied to both the fossil and modern samples.

[insert Table 1 here]

2.2 Methods

2.2.1 SEM-EDS

Uncoated samples were analyzed using a scanning electron microscope (SEM) JEOL JSM6610LV with backscatter detection (BSE) and equipped with an energy-dispersive X-ray spectroscopy detector (EDS) controlled by the software OXFORD

INSTRUMENTS X-MAX at the University of São Paulo (Ribeirão Preto). Prior to analysis, samples were polished using silicon carbide papers ranging from 320 to 2500 grit. Analyses were conducted at 20 kV, with spot size between 71 to 78 µm, and working distance ranging from 8 to 15 mm. Elemental maps and point spectra were collected from different parts of bone/teeth, including vascular canals and cracks, and analyzed in the software AZtec 3.0 SP1.

2.2.2 Micro-Raman spectroscopy

A Renishaw InVia micro-Raman spectrometer (AstroLab, University of São Paulo) coupled to 532 and 785 nm lasers with the static measurement mode was used to investigate a broad range of mineral phases, including apatites, oxides, and carbonates. Different powers and times were tested to obtain the most informative spectra. We adjusted parameters according to 25 mW, using an LW 50x objective, with 30 accumulations of 2 seconds each. The software SpectraGryph 1.2 was used for the treatment and identification of Raman vibrational bands. We normalized (0–1) and subtracted the baseline of all spectra. The raw data were considered for those spectra whose fluorescence and luminescence effects were enhanced with this type of treatment. Mineral standards, the *RRUFF* database (Lafuente et al., 2015), and spectra described in the literature (Table 2) were used to compare and thus identify the bands obtained in the material studied.

2.2.3 XRF

XRF analyses were conducted using a portable EDXRF system composed of an Amptek silver (Ag) X-ray tube and an Amptek Silicon XR-100SDD FAST detector at the Laboratory of Archaeometry and Sciences Applied to Cultural Heritage (LACAPC), University of São Paulo (USP). Measurements were performed directly on the samples using a voltage of 30 kV, a current of 5 µA, and an acquisition time of 300s (without collimator). Data fitting was performed using a Windows version of the software system QXAS (WinQXAS 1.4), developed by the International Atomic Energy Agency (IAEA).

2.2.4 XRD

Mineralogical analysis was performed using a D8 Bruker diffractometer (Laboratory of X-ray diffraction, Institute of Geosciences, University of São Paulo). The diffractometer operated at a voltage of 40 kV and a current of 40 mA. The angular step size used was 0.02 degrees 2-theta in the interval from 4 to 65 degrees 2-theta. XRD data were interpreted using HighScore Plus 5.0 software (Panalytical). The Crystallographic Open Database (COD, Grazulis et al., 2009) was used as a reference for identifying mineral phases. The Rietveld method (Rietveld, 1967) was employed for quantitative phase analysis using HighScore Plus 5.0 software; refined parameters were scale factor, cell parameters, peak broadening, asymmetry, shape, and preferential orientation.

3. Results

3.1 Elemental composition (XRF and SEM-EDS)

XRF and SEM-EDS analyses consistently revealed contrasting elemental compositions between the fossil skeletal remains and their host matrix (Fig. 2, Fig. 3, Fig. S.1; Table S.1; Table S.2). As expected, both techniques showed elevated counts of calcium (Ca) and phosphorus (P) in the fossil bones and teeth, reflecting their apatite composition (Fig. 2, Fig. 3). SEM-EDS elemental maps further confirmed the homogeneous distribution of Ca, P, and oxygen (O) within the fossil skeletal remains.

In addition, EDS analyses identified the presence of fluorine (F), sodium (Na), magnesium (Mg), strontium (Sr), and cerium (Ce) in the sampled areas of fossil bones and teeth. XRF data also indicated an overall enrichment of several trace elements in fossil samples compared to modern crocodylian samples, including manganese (Mn), strontium (Sr), yttrium (Y), barium (Ba), cerium (Ce) and thorium (Th), which were either absent or occurred at very low levels in recent samples (Fig. 2; Table S.2). Among fossil samples, elements such as Mn, Fe, Sr, Y, Ba, and Ce have generally higher counts in bone than in teeth, with enamel typically displaying the lowest counts (Fig. 2).

The four most abundant void-filling elements within fossil bones and teeth were manganese, cerium, iron, and calcium (Table S.1). Of the 27 fossil samples mapped by SEM-EDS analysis, manganese was the most frequent void-filling element, occurring in vascular canals and cracks of 21 samples (77%), often resulting in darker staining in isolated teeth (LPRP/USP 0794, MPPC SN). Cerium was detected in similar voids in 20 samples (74%), while iron occurred in eight samples (29%). In six samples (22%), the vascular canals and fractures were filled with a mineral rich in Ca and O, but deficient in P, consistent with calcite. These calcite infillings, notably in LPRP/USP 0786 (long bone), LPRP/USP 0791 (osteoderm), and LPRP/USP 0050 (vertebra), are often associated with the presence of micro-fracturing in cortical and cancellous bone (Fig. 4).

The host rocks, as confirmed by both XRF and SEM-EDS, are compositionally distinct from the fossil material, showing higher levels of silicon (Si), aluminum (Al), potassium (K), and iron (Fe). XRF results also revealed elevated counts of titanium (Ti), chromium (Cr), copper (Cu), rubidium (Rb), and zirconium (Zr) in the rock samples. Although the elements Fe, K, and zinc (Zn) had higher counts in the rock samples, they were also detected in fossil bones and teeth via XRF analysis.

[insert Figure 2 here]

[insert Figure 3 here]

[insert Figure 4 here]

3.3 XRD

The XRD patterns of fossil specimens and associated rock matrix are shown in Figure S.2. Measured percentages of the mineral composition of the samples are presented in Table S.3. Fluorapatite is confirmed as the main mineral phase of the fossil bone and tooth samples (93.7–100%). Secondary minerals were also identified in these samples and include quartz (0.8–2.3%), calcite (0.2–2.8%), siderite (0.4–1.2%), goethite (1.5%), and pyrolusite (1.1%). Rock samples are mainly composed of quartz (51.9–75.7%) and might include illite (3–16%), vermiculite (3.2–13.6%), calcite (1.7–33.2%), plagioclase (5.5–17.6%), clinopyroxene (2.4–13.1%), goethite (1.5%), and sylvite (0.3%). Sample 7 (LPRP/USP 0050; Fig. S.3) is a mixture of fossil bone and encasing rock, which explains the low abundance of fluorapatite (8%) and the identification of quartz, vermiculite, and analcime.

3.4 Micro-Raman

We obtained Raman spectra in the 200–3800 cm^{-1} range for modern and fossil skeletal tissues and rocks. Figure 5 shows representative spectra from the analyzed samples. The main peaks are attributed to characteristic vibrations of phosphate, carbonate, and collagen (Fig. 5, Table 2). In modern bone, the most intense band at 960 cm^{-1} represents the $\nu1(PO_4)$ symmetrical stretching mode of the phosphate in apatite. The ν2(PO_4) and ν4(PO_4) bending modes were also observed near 430 cm^{-1} and 582 cm^{-1}, respectively. A strong band near 1071 cm^{-1} is compatible with the ν1(CO_3) mode of carbonate ions occupying phosphate sites (B-type substitution). Besides the peaks associated with the mineral portion of the modern bone, less intense bands related to collagen vibrations were also identified: proline (851–854 cm^{-1}), phenylalanine (~1002 cm^{-1}), amide III (1239–1247 cm^{-1}), amide I (1650–1690 cm^{-1}), and C-H bending and stretching modes (1447–1452 cm^{-1} and 2800–3060 cm^{-1}, respectively) (Table 2).

The typical ν1, ν2, and ν4 modes of PO_4 and the ν1 mode of CO_3 (B-type) were observed in static spectra (200–1300 cm^{-1}) for both modern tooth enamel and dentine. The ν1(PO_4) mode in the modern tooth spectra was slightly shifted to lower frequencies compared to modern bone, located at 959.6 ± 1.2 cm^{-1}. Organic bands were barely detected in the static spectra, except for proline peaks in a few spectra. An extended spectrum, however, showed that all main organic peaks are present in the dentine of the modern specimen (Fig.5). The organic bands in the extended spectrum of the enamel are weaker or not detectable, except for a distinct peak at ~2940 cm^{-1} related to the C-H stretching mode (Fig.5B).

[insert Table 2 here]

The selected crocodyliform fossils have variations in their Raman spectra, with recovered values more scattered and sometimes shifted in comparison to the analyzed modern bone and teeth (Fig. 5, Fig. 6, Fig. S.5; Table S.4). The ν1(PO_4) peak in the fossils is shifted to higher frequencies, presenting narrower bands (smaller FWHM values) (Fig. S.5). Raman spectra from the modern bone had an average ν1(PO_4) peak position at 960.4 ±0.2 cm^{-1} and width of 17.8 [0.2] cm^{-1}. Slightly lower values were found for the modern tooth, with the mean ν1(PO_4) peak location at 959.6 ±1.2 cm^{-1} and width of 15.1 ±1 cm-

^{1}. By contrast, the average ν1(PO$_4$) peak position and width were 964.1 ±2 cm^{-1} and 12.1 ±1.1 cm^{-1}, respectively, for fossil specimens. Other bands assigned to phosphate (ν2 and ν4) and carbonate (ν1) vibration modes in modern apatite were also detected in static spectra of the fossil bones and teeth, although some were not observed in extended spectra (Fig. 5A).

In contrast to the Raman spectra of the modern crocodylian bone and tooth, the spectra from the fossil specimens show an overall loss of organic bands. Peaks related to collagen vibrations, such as amide I, amide III, and C-H stretch, are not visible in any of the fossil spectra (Fig. 5). We have detected a peak at ~850 cm^{-1} in the extended spectrum of *A. escharafacies* which could be assigned to proline, however, this peak was not observed in the static spectra. Very low-intensity peaks at ~1005 cm^{-1} (*Mariliasuchus*) and ~1010 cm^{-1} (*Mariliasuchus*, *P. sera*) resemble that of phenylalanine (~1002 cm^{-1}), but they appear at higher frequencies and are only apparent after data processing (baseline correction, smoothing). Also, putative organic peaks related to C-H bending (~1450 cm^{-1}) are observed in the extended spectra of *A. sordidus*, *A. escharafacies*, *P. sera,* and the dentine of an indeterminate fossil crocodyliform tooth.

Extended spectra from the external bone cortex of *P. sera* and the dentine of an isolated tooth recorded some intense and broad bands between the 1200–1800 cm^{-1} interval, with the main peaks occurring at ~1190 cm^{-1}, ~1270 cm^{-1}, ~1403 cm^{-1}, ~1540 cm^{-1}, and 1670 cm^{-1} (Fig. 7). The identification of these bands in fossils are still unclear and different explanations have been proposed (Jurašeková et al., 2022; Sousa et al., 2024; see Discussion). Raman spectra from rock samples associated with the fossil specimens only showed characteristic peaks of common minerals such as quartz, hematite, calcite, and silicates (Table 2; Table S.5).

[insert Figure 5 here]

[insert Figure 6 here]

[insert Figure 7 here]

4. Discussion

4.1 Effects of diagenesis on bioapatite structure and composition

The bioapatite lattice is flexible, allowing substitutions at every site (Ca^{2+}, PO_4^{3-}, OH^-) (Pan and Fleet, 2002; Kohn, 2008; Fig. 8E). Although some substitutions take place *in vivo*, substantial compositional alterations occur during recrystallization after the loss of protective collagen and exposure of crystallites to pore fluids (Weiner and Price, 1986; Hubert et al., 1996; Trueman, 1999; Kohn and Cerling, 2002; Trueman and Tuross, 2002; Berna et al., 2004; Pfretzschner, 2004; Trueman et al., 2004; Chinsamy-Turan, 2005; Trueman et al., 2006; Kohn, 2008; Trueman et al., 2008; Koenig et al., 2009; Rogers et al., 2010; Suarez et al., 2010; Keenan, 2016; Keenan and Engel, 2017; Ullmann et al., 2020; Cowen et al., 2025; Ullman et al., 2025). Common Ca^{2+} substitutions include alkaline-earth metals (Mg^{2+}, Sr^{2+}, Ba^{2+}), Mn^{2+}, Na^+, K^+, and rare earth elements (REEs), PO_4^{3-} can be replaced by CO_3^{2-} (B-type) or other anions, and OH^- is often substituted by F^-, Cl^-, and CO_3^{2-} (A-type) (Hubert et al., 1996; Elliot, 2002; Pan and Fleet, 2002; Trueman and Tuross, 2002; Wopenka and Pasteris, 2005). The incorporation of foreign ions is influenced by many variables, such as ion availability and extent of pore fluid interactions, charge balance within the lattice, ion radius, and electrostatic repulsion (e.g., Keenan and Engel, 2017; Ullmann et al., 2020).

SEM-EDS spectra have shown the ubiquitous presence of Ca, P, and O in fossil bones and teeth, reflecting the original apatite chemical composition. XRF analyses also confirmed the high intensities of Ca and P in the fossil specimens. Na, Mg, Sr, and Ce were detected by EDS associated with the apatite signal, probably replacing the Ca lattice sites (Keenan, 2016; Keenan and Engel, 2017). The presence of Sr and Ce agrees with XRF results, which also showed higher counts of Mn and Fe in the fossil samples. However, because the samples analyzed by XRF were in powdered form, it is hard to tell to what extent the intensities of Mn, Fe, and Ce are more representative of void filling by authigenic minerals than substitutions of Ca^{2+} for other ions in the apatite structure. XRF data show that, on average, fossil enamel exhibited lower counts of foreign ions compared to fossil bone and dentine, consistent with its greater resistance to diagenetic alteration due to higher crystallinity and lower porosity (Kohn and Cerling, 2002; Koch, 2007; Kendall et al., 2018).

Cerium was the only REE confidently detected by EDS, likely reflecting a high concentration in the fossils. The XRF results were able to detect two other REEs in many of the fossil samples: Y and Eu. Among the REEs, Ce and Eu are uniquely redox-sensitive and have been used as proxies to infer environmental redox conditions during fossilization (e.g., Trueman and Tuross, 2002; Suarez et al., 2010; Chen et al., 2015; Gueriau et al., 2015; McLain et al., 2021; Ullmann et al., 2025). However, interpreting deviations in their concentrations and their implications for redox conditions requires higher-resolution analyses of broader REEs patterns (e.g., Trueman and Tuross, 2002; Herwartz et al., 2013; McLain et al., 2021). Additionally, the detection of fluorine (F) in fossil bioapatite by EDS indicates substitutions at the OH^- sites and the precipitation of fluorapatite.

The rapid recrystallization of bioapatite into a more stable phase is crucial for the long-term survival of fossil elements. Actualistic studies have shown that this process begins early in diagenesis, sometimes even before burial (Trueman et al., 2004; Keenan and Engel, 2017). Hydroxyapatite is unstable in many burial environments and tends to dissolve unless it is transformed into a more thermodynamically stable mineral, such as carbonated fluorapatite or fluorapatite (Berna et al., 2004; Keenan and Engel, 2017; Keenan, 2023). It has been demonstrated that fluorapatite and carbonated fluorapatite stability shift toward supersaturation under lower P concentrations and pH conditions compared to that of hydroxyapatite (Keenan and Engel, 2017). Thus, it is not surprising that fluoridation of bioapatite is such a widespread process, documented in many Mesozoic vertebrate fossils, including specimens from the Bauru Group (Fernandes and Ribeiro, 2015; Marchetti et al., 2019; Pinto et al., 2020; Klock et al., 2022).

Raman spectroscopy is highly sensitive, enabling the detection of alterations in bioapatite chemistry and structure. Changes caused during fossilization can be mainly monitored based on the position and the width of the $\nu1(PO_4)$ peak. Dislocation of the $\nu1(PO_4)$ peak position indicates that ionic substitutions produced shorter P-O bond lengths and smaller unit cells (blueshifts) or longer P-O bond lengths and larger unit cells (redshifts) (Kannan et al., 2007; Campillo et al., 2010; Thomas et al., 2011; Sousa et al., 2020). Experimental works have identified the type and degree of dislocation of specific ionic substitutions (Thomas et al., 2007, 2011). Progressive redshifted positions were observed with increasing incorporation of Sr^{2+}, CO_3^{2-}, and other ions into the apatite lattice, whereas the incorporation of F^- resulted in blueshifts (Thomas et al., 2011; Fig. 6). The smaller ionic radius of F^- compared to OH^- results in a contraction of the unit cell in the a-axis plane and an increase in the crystal size (LeGeros, 1981; Kannan et al., 2007;

Fig. 8D, E), which contributes to the higher thermodynamic stability of fluorapatite in relation to hydroxyapatite (Berna et al., 2004).

The Raman spectra obtained for modern crocodylian bone and tooth had an average ν1(PO_4) peak position of 960.4 ± 0.2 cm^{-1} and 959.6 ± 1.2 cm^{-1}, respectively, which is redshifted compared to synthetic and abiotic hydroxyapatite, and matches more closely the values for synthetic carbonated apatite (Fig. 6; Thomas et al., 2011). This result is expected because bones and teeth are naturally enriched in CO_3^{2-} ions (A-type and B-type substitutions). All ν1(PO_4) peak positions of fossil specimens are blueshifted, consistent with fluoridation and transformation or replacement of the original carbonated hydroxyapatite to fluorapatite, supporting our EDS and XRD results (Fig. 6, Fig. S.5).

The FWHM (full-width half maximum) of the ν1(PO_4) peak has been used as a proxy to assess the degree of apatite crystallinity, with FWHM values being inversely proportional to crystallinity (Thomas et al., 2007; Zhang et al., 2017; Sousa et al., 2020). Carbonate substitutions significantly decrease crystallinity (De Mul et al., 1988; Berna et al., 2004; Dal Sasso et al., 2018a,b), with non-carbonated hydroxyapatites and fluorapatites (synthetic and magmatic) displaying narrower bands than carbonated apatites (synthetic and bioapatite) (Thomas et al., 2011; Fig. 6). Although apatite crystallinity increases with the loss of carbonate ions, its lattice is substantially enriched by trace elements during diagenesis, which should increase atomic disorder. However, this is counter-balanced by structural rearrangements of these ions that can narrow the FWHM of fossil specimens (Zhang et al., 2017).

As expected, the fossil crocodyliform bone and tooth apatites revealed narrower bands (FWHM = ~12.1 cm^{-1}) compared to the recent ones (FWHM = ~17.8 for bones and ~15.1 for teeth). While the band position of the ν1(PO_4) peak shows a clear trend of fossil specimens toward fluoridation, they are less crystalline than synthetic and magmatic fluorapatites (Fig. 6). One of the possible explanations is the maintained influence of carbonate in the fluorapatite structure in reducing crystallinity, as evidenced by the detection of the carbonate (ν1) vibration mode at around 1070 cm^{-1} in all analyzed fossil samples (Fig. 5A). Also, geological and synthetic apatites might crystallize at higher temperatures which favor increased crystallinity (Pang and Bao, 2003; Takeuchi et al., 2009; Chen et al., 2017).

No significant overall correlation was found between the ν1(PO_4) peak position and width (FWHM) ($r = 0.11$, $p = 0.28$; Fig. S.6D). Increased F^- incorporation generally reflects in shifts to higher frequencies and smaller FWHM values due to the formation of larger crystal sizes (e.g., Barthel et al., 2020). However, the diagenetic history for each specimen is complex and involves exposure to different pore-water chemical compositions and probably different rates and modes of recrystallization. Specimens can incorporate or release varying amounts of different ions (e.g., CO_3, Sr^{2+}), each adding competing trends to the ν1(PO_4) peak position and FWHM (Thomas et al., 2007, 2011; Zhang et al., 2017).

The heterogeneity of the phosphate stretching environment is also illustrated when the relationship between the ν1(PO_4) peak position and width (FWHM) considers only the Raman spectra collected for each specimen. We found a negative correlation between these two parameters in the samples from *Mariliasuchus* ($r = -0.77$, $p < 0.05$) and *P. sera* (LPRP/USP 0049A; $r = -0.64$, $p < 0.05$) (Fig. S.6A, B), which probably reflects the effect of a predominant substitution type. Other samples demonstrate very weak and non-significant relationships between the variables, such as for *P. sera* (LPRP/USP 0050; $r = 0.12$, $p = 0.12$; Fig. S.6C). This diverging pattern probably indicates a more heterogeneous ionic environment in the fossil apatite samples.

We tentatively explored the effect of Sr enrichment in the ν1(PO_4) peak position of the studied fossil bones, using the ratio of Sr/P counts based on XRF results (Table S.6). We found a negative correlation between the two variables (r = -0.83, p = 0.08), which is in accordance with previous studies suggesting a redshift effect of Sr^{2+} in the apatite lattice (Thomas et al., 2011). However, the correlation did not reach statistical significance, and this relationship might be worthy of further investigation in future studies exploring larger sample sizes of fossil specimens.

[insert Figure 8 here]

4.2 Permineralization indicates alkaline and oxidative pore waters

The majority (more than 80%) of specimens mapped with EDS showed high intensities of Ca, Fe, Mn, and Ce in void spaces (Figs. 3, 4; Fig. S.1). The identification of related minerals was possible in a few samples based on micro-Raman and XRD. The presence of calcite as a void-filler has been confirmed by Raman analysis of two bone samples (LPRP/USP 0049A and 0050; Fig. S.4). XRD confirmed our micro-Raman results, showing that most fossil skeletal samples contain calcite. Iron and manganese minerals were detected in only one sample (LPRP/USP 0794) and identified as goethite and pyrolusite, respectively. The XRD results also indicated the presence of siderite in half of the analyzed fossil samples.

Mn oxides and Fe (hydr)oxides are common void-filling materials in vertebrate fossils (Pfretzschner, 2004; Schweitzer et al., 2014; Boatman et al., 2019). Their formation is often associated with late or post-diagenetic processes. Under seasonal wet/dry climates and alkaline oxidizing microenvironments, mobile ions (Fe^{2+}, Mn^{2+}) can infiltrate empty cavities in periods of water saturation and precipitate as highly insoluble oxides during dry periods (Pereda-Superbiola et al., 2000; Luque et al., 2009; Tomassini et al., 2014; Previtera et al., 2016; Fig. 8A-C). Organic degradation and microbial activity may also play a role in their precipitation (Pfretzschner and Tütken, 2011; Santelli et al., 2011; Owocki et al., 2016). For instance, iron can precipitate first as pyrite (FeS_2) within bone voids under low redox conditions generated by organic decay and sulfide production mediated by sulfate-reducing bacteria (Berner, 1984; Canfield and Raiswell, 1991; Pfretzschner, 2004; Vietti et al., 2015; Bosio et al., 2021), which may later oxidize into iron (hydro)oxides (Pfretzschner, 2001a,b; 2004; Rogers et al., 2020; Laker, 2024). Iron may also derive from endogenous sources, such as the degradation of hemoglobin and other iron-bearing biomolecules during early diagenesis. This process can lead to localized iron precipitation and potentially facilitate the preservation of biomolecules in fossils (Schweitzer et al., 2014; Boatman et al., 2019).

Cerium (Ce) is notably present in bone/tooth voids in the majority of analyzed samples (74%). While bioapatite can incorporate Ce and other REEs during fossilization (Trueman and Tuross, 2002; Keenan, 2016; Keenan and Engel, 2017), they are rarely mentioned as important void-filling materials. Under oxidizing conditions, Ce can be oxidized to CeO_2 or adsorbed onto Fe and Mn (hydro)oxides (Koeppenkastrop and De Carlo, 1993; Suarez et al., 2010; Suarez et al., 2018). EDS maps show Ce-enriched voids sometimes co-occurring with Fe and Mn-bearing minerals (Fig. 3; Fig. S.1), suggesting CeO_2 formation or adsorption onto Mn/Fe (hydro)oxides. Additionally, Ce may be incorporated into calcium carbonate minerals by substituting for Ca^{2+} (e.g., Zhao et al., 2021).

Fossil bone voids are frequently filled by calcite (e.g., Hubert et al., 1996; Holz and Schultz, 1998; Pfretzchner, 2004; Wings, 2004; Riga and Astini, 2007; Luque et al., 2009; Rogers et al., 2020). It has been identified in more than 20% of analyzed samples.

The formation of calcite is associated with rapid evaporation of meteoric waters and variations in the phreatic level, which supplies bone and teeth with alkaline CaCO3-enriched pore waters (Wright and Tucker, 1991; Holz and Schultz, 1998; Dal Sasso et al., 2014). The interior of some specimens (Fig. 4) showed bone fragments 'floating' or significantly displaced while surrounded by the calcite matrix. It is possible that these bones suffered a less severe version of the diagenetic alterations described in Brazilian Triassic fossils (Holz and Schultz, 1998). Holz and Schultz (1998) suggested that the swelling and deformation observed in their studied fossil bones resulted from the displacive growth of calcite crystals. This process was probably fostered by the rapid calcite precipitation in a marked seasonal arid climate during early diagenesis when lithostatic pressure was still low (Watts, 1978; Holz and Schultz, 1998). Although the occurrence of displacive calcite caused by the force of crystallization has been broadly discussed in the geological literature (e.g., Watts, 1978; Buczynski and Chafetz, 1987; Monger and Daugherty, 1991; Meng et al., 2018; Su et al., 2022), its effect in bone/tooth diagenesis has been poorly explored (Holz and Schultz, 1998; Goldberg and Garcia, 2000; Pérez et al., 2022).

The detection of siderite in some fossil samples is intriguing as it can be interpreted as relict evidence of the initial dysoxic to anoxic and relatively reducing conditions imposed by organic decay in early diagenesis (Wings, 2004). Siderite precipitation commonly occurs in environments with low redox potential, slightly alkaline pH, and a high concentration of iron (Clarke and Barker, 1993; Farlow and Argast, 2006), potentially mediated by iron and sulfate-reducing bacteria (Mortimer et al., 1997; Lim et al., 2004; Lin et al., 2020). The subsequent increase in alkalinity might have favored the precipitation of calcite instead of siderite (Roberts et al., 2013), while exposure to oxidizing conditions might be responsible for the overall dissolution of siderite, which was probably reprecipitated as iron oxide (Senkayi et al., 1986; Bao et al., 1998; Loope et al., 2012).

While the exact pathways and timing (e.g., early vs. late diagenesis) for the permineralization process in the fossils need to be further investigated, the detected mineral infills are consistent with prevailing alkaline and oxidizing pore waters under the influence of intense evaporation and/or water table fluctuations.

4.3 Raman micro-spectroscopy: possible organic peaks and enigmatic compounds

Although we obtained peaks in the 800–1500 cm^{-1} interval suggestive of organic compounds, they are generally poorly defined with low relative intensity and/or are associated with possible luminescence effects (Fig. 5A). Therefore, in the absence of more detailed and independent molecular analyses, the presence of organic compounds in the analyzed fossils is not assumed.

The very intense and broad peaks occurring in the 1000–1800 cm^{-1} region in the spectra of *P. sera* (LPRP/USP 0050, vertebra) and the dentine of an isolated fossil tooth (LPRP/USP 0794) represent still enigmatic compounds (Fig. 7). They are located in the Raman region where some known organic bands of bone and teeth appear, but differ in terms of intensity, position, and width. Similar bands have been found in fossils from different locations and ages (Yang and Wang, 2007; Piga et al., 2011; Marshall et al., 2012; Barros et al., 2019; Wang et al., 2020; Korneisel et al., 2021; Jurašeková et al., 2022; Sánchez-Pastor et al., 2024; Sousa et al., 2024). Marshall et al. (2012) studied the body parts and gut nodules of Cambrian arthropods from the USA and found that the body parts contained D and G bands of carbonaceous material. The gut nodules, however, showed similar intense bands between 1000–1800 cm$^{-1,}$ which were attributed to large-ring clusters of polycyclic aromatic hydrocarbons (PAHs). PAHs are stable products of the geochemical maturation of organic compounds that can become progressively carbonized and graphitized, being ultimately transformed into graphite (e.g., Durand, 1980; Wopenka and Pasteris, 1993; Schopf et al., 2005). Nevertheless, the enigmatic peaks do not closely match those of carbonaceous D and G bands (Fig. 7), nor those of published PAHs in Raman spectra (Chen et al., 2014; Cloutis et al., 2016; Jurašeková et al., 2022).

An alternative interpretation has been proposed by Korneisel et al. (2021) based on the chemical composition of secondarily-infilled vascular canals in a bone of a Cretaceous theropod from China. EDS and TOF-SIMS results demonstrated that a mixture of clay minerals and carbonaceous compounds filled these vascular canals. The peaks in the 1000–1800 cm^{-1} region were considered photoluminescent bands generated by rare earth elements related to the fossil bone apatite.

Jurašeková et al. (2022) suggested that the unknown bands have features that could be consistent with both inorganic and organic compounds. While the authors do not entirely reject PAHs or a mixture of clay minerals and carbonaceous compounds as possible identifications, they suggest that the bands are most probably associated with a highly transformed carbonate-rich compound. Similar bands have been recently described in Pleistocene vertebrate fossils from Brazil and interpreted as organic compounds related to fossilized biofilm (Sousa et al., 2024). Notably, however, neither Jurašeková et al. (2022) nor Sousa et al. (2024) explicitly address the hypothesis that these bands might represent photoluminescent bands created by REEs in apatite, as similarly observed in geological and synthetic apatites (Culka and Jehlička, 2018; Fau et al., 2022; Fig. 7). The observed bands closely resemble the fluorescence pattern in minerals naturally enriched or intentionally doped with Nd^{3+} ions (Chen and Stimets, 2014; Fau et al., 2022). Similar signals have also been reported in bones subjected to *in vitro* aqueous experiments, where they were associated with the absorption of Nd^{3+} ions in apatite (Kral et al., 2022). It is evident that the interpretation of the enigmatic bands as organic compounds remains uncertain. Further chemical analyses using complementary techniques (e.g., LA-ICPMS, TOF-SIMS, immunoassays) would help clarify this issue.

4.4 Wider implications for fossil bioapatite studies

The chemical composition of fossil bioapatite has been used as a proxy for a wide range of past reconstructions, including environmental, ecological, and chronological aspects of fossil specimens (e.g., Kohn and Cerling, 2002; Trueman and Tuross, 2002; Fricke, 2007; Trueman and Moore, 2007; Koch, 2007; Tütken et al., 2011; Cullen et al., 2022; Martin et al., 2022; Klock et al., 2022). Because diagenetic alterations can overprint signatures of interest (e.g., Kolodny et al., 1996; Trueman et al., 2003; Lécuyer et al., 2003; Tütken and Vennemann, 2011; Suarez and Kohn, 2020), several methodologies have been proposed to assess the degree of modification of fossil bioapatite and to evaluate the reliability of chemical results (e.g., Kolodny et al., 1996; Thomas et al., 2007; Thomas et al., 2011; Tütken and Vennemann, 2011).

Thomas et al. (2007, 2011) have demonstrated that Raman spectroscopy can be promising for verifying diagenetic changes in bioapatite and determining if original isotopic compositions are significantly shifted. For instance, based on phosphate-oxygen isotopes ($\delta^{18}O_p$) of paired enamel and dentine samples from a broad selection of fossils, Thomas et al. (2011) defined an alteration field based on $\nu1(PO_4)$ spectral parameters where the diagenetic alteration was enough to change the original oxygen isotope composition significantly. The only analyzed fossil enamel in this study has a mean $\nu1(PO_4)$ peak position of 963.7 cm^{-1} and a FWHM of 11.1 cm^{-1}, which falls outside the proposed diagenetic alteration field (Fig. 6). The mean $\nu1(PO_4)$ peak position of fossil bones is higher (964.5 cm^{-1}) and reinforces the idea that bone apatite is more susceptible to diagenetic modifications than enamel apatite due to its structural properties, making it less preferable for isotopic analyses (Lee-Thorp and van der Merwe, 1991; Ayliffe et al., 1994; Kohn et al., 1999; King et al., 2011; Kendall et al., 2018). Nevertheless, the utility of the alteration field proposed by Thomas et al. (2011) to pre-screen samples would benefit from the inclusion of additional samples with a wider variety of diagenetic histories.

5. Conclusions

Diagenetic features of fossil crocodyliforms from the Adamantina Formation were investigated using SEM-EDS, XRF, XRD, and micro-Raman spectroscopy. We have shown that the fossilization of bones and teeth involved significant compositional and structural changes, such as the overall loss of organic matrix, permineralization of voids, substitutions by different ions, and recrystallization. The transformation of the bioapatite (carbonated hydroxyapatite) into carbonated fluorapatite in all studied samples reinforces the importance of the establishment of a more thermodynamically stable mineral phase for the survival of skeletal remains over geological time scales. Authigenic void-filling minerals are consistent with significant interactions with alkaline and oxidizing pore waters under an arid to semi-arid environment. However, the occurrence of displacive calcite and evidence for “relict” siderite in some specimens point to a higher complexity in the interaction of bones and teeth with diagenetic fluids. The Adamantina Formation fossil specimens also display different Raman spectral signals consistent with different modes of diagenetic alteration and effects on crystallinity. Some spectral values suggest intense recrystallization that might have modified the element's isotopic compositions. Nevertheless, results for the enamel of a fossil tooth presented good preservation indicators, supporting the potential of this type of tissue to retain biogenic signals. The combination of techniques applied in this study provided a comprehensive understanding of the diagenetic modifications of crocodyliform skeletal elements, which can potentially inform sampling strategies for more costly and time-consuming analyses (e.g., molecular tests and isotopic studies).

Acknowledgments

This research was supported by Coordenação de Aperfeiçoamento de Pessoal de Nível Superior (CAPES 001), Conselho Nacional de Desenvolvimento Científico e Tecnológico (CNPq No. 315692/2023-5), and by the São Paulo Research Foundation (FAPESP No. 2020/07997-4; No. 2024/03599-5; No. 2021/07007-7; No. 2022/06485-5; No. 2023/14250-0; No. 23/04501-6). Gabriel Osés thanks the Programa de Pós-Doutorado and the Programa de Pesquisador Colaborador of the Institute of Physics, University of São Paulo. We are also grateful to Max Langer and Fabiano Iori for kindly providing access to fossil specimens used in this study, and to Fernando Ibanez Martins for collecting and sending us skull and teeth samples from a modern crocodylian. Adam Culka kindly provided the reference spectrum of a mineral apatite with fluorescent bands. We thank Guilherme Hermanson for his help with one of the figures, and Friedrich Menges for freely providing the software Spectragryph (http://spectragryph.com/). Finally, we thank the Editor-in-Chief, Maria Rose Petrizzo, and the reviewers (Giulia Bosio and an anonymous one) for their suggestions that improved the manuscript.

During the preparation of this work the authors used ChatGPT from OpenAI and Grammarly in order to revise the grammar of the manuscript. After using this tool/service, the authors reviewed and edited the content as needed and take full responsibility for the content of the published article.

References

Alebrahim, M., Krafft, C., Sekhaneh, W., Sigusch, B., Popp, J., 2014. ATR-FTIR and Raman spectroscopy of primary and permanent teeth. Biomed. Spectrosc. Ima. 3, 15–27.

Alvarez, B.N., Casal, G.A., Ibiricu, L.M., Tomas, A.D.S., Suarez, C.A., 2022. Insights into paleoecology of the Bajo Barreal Formation (Upper Cretaceous), Patagonia, Argentina. J. S. Am. Earth Sci. 116, 103854.

Arai, M., Fernandes, L.A., 2023. Lower Campanian palynoflora from the Araçatuba Formation (Bauru group), southeastern Brazil. Cretac. Res. 150, 105586.

Araújo-Júnior, H.I., Marinho, T., 2013. Taphonomy of a *Baurusuchus* (Crocodyliformes, Baurusuchidae) from the Adamantina Formation (Upper Cretaceous, Bauru Basin), Brazil: implications for preservational modes, time resolution, and paleoecology. J. S. Am. Earth Sci. 47, 90–99.

Ayliffe, L.K., Chivas, A.R., Leakey, M.G., 1994. The retention of primary oxygen isotope compositions of fossil elephant skeletal phosphate. Geochim. Cosmochim. Acta 58, 5291–5298.

Azevedo, K.L., 2012. Aspectos tafonômicos de vertebrados da parte oriental do Grupo Bauru, Cretáceo Superior [Master’s thesis]. Universidade Federal do Paraná.

Azevedo, K.L., Vega, C.S., Fernandes, L.A., 2013. Taphonomic aspects of vertebrate fossils from Bauru Group, Upper Cretaceous, Brazil. Bol. Parana. Geociências 68-69. 43–51.

Bandeira, K.L., Brum, A.S., Pêgas, R.V., Cidade, G.M., Holgado, B., Cidade, A., Souza, R.G., 2018. The Baurusuchidae vs Theropoda record in the Bauru Group (Upper Cretaceous, Brazil): a taphonomic perspective. J. Iber. Geol. 44, 25–54.

Bao, H., Koch, P.L., Hepple, R.P., 1998. Hematite and calcite coatings on fossil vertebrates. J. Sediment. Res. 68, 727–738.

Barros, O.A., Silva, J.H., Saraiva, G.D., Viana, B.C., Paschoal, A.R., Freire, P.T.C., Oliveira, N., Paula, A., Viana, M.S., 2019. Physicochemical investigation of shrimp fossils from the Romualdo and Ipubi formations (Araripe Basin). PeerJ 7, e6323.

Barthel, H.J., Fougerouse, D., Geisler, T., Rust, J., 2020. Fluoridation of a lizard bone embedded in Dominican amber suggests open-system behavior. Plos one 15, e0228843.

Basilici, G., Dal'Bo, P.F., Oliveira, E.F., 2016. Distribution of palaeosols and deposits in the temporal evolution of a semiarid fluvial distributary system (Bauru Group, Upper Cretaceous, SE Brazil). Sediment. Geol. 341, 245–264.

Batezelli, A., 2015. Continental systems tracts of the Brazilian Cretaceous Bauru Basin and their relationship with the tectonic and climatic evolution of South America. Basin Res. 29, 1–25.

Batezelli, A., Ladeira, F.S.B., Nascimento, D.L.D., Da Silva, M.L., 2019. Facies and palaeosol analysis in a progradational distributive fluvial system from the Campanian–Maastrichtian Bauru Group, Brazil. Sedimentology 66, 699–735.

Berna, F., Matthews, A., Weiner, S., 2004. Solubilities of bone mineral from archaeological sites: the recrystallization window. J. Archaeol. Sci. 31, 867–882.

Berner, R.A., 1984. Sedimentary pyrite formation: an update. Geochim. Cosmochim. Acta 48, 605–615.

Bērziņš, K., Sutton, J.J., Loch, C., Beckett, D., Wheeler, B.J., Drummond, B.K., Fraser-Miller, S.J., Gordon, K.C., 2019. Application of low-wavenumber Raman spectroscopy to the analysis of human teeth. J. Raman Spectrosc. 50, 1375–1387.

Boatman, E., Goodwin, M., Holman, H., Fakra, S., Zheng, W., Gronsky, R., Schweitzer, M., 2019. Mechanisms of soft tissue and protein preservation in Tyrannosaurus rex. Sci. Rep. 9, 15678.

Bosio, G., Gioncada, A., Gariboldi, K., Bonaccorsi, E., Collareta, A., Pasero, M., Celma, C., Malinverno, E., Urbina, M., Bianucci, G., 2021. Mineralogical and geochemical characterization of fossil bones from a Miocene marine Konservat-Lagerstätte. J. S. Am. Earth Sci. 105, 102924.

Buczynski, C., Chafetz, H.S., 1987. Siliciclastic grain breakage and displacement due to carbonate crystal growth: an example from the Lueder's Formation (Permian) of north-central Texas, USA. Sedimentology 34, 837–843.

Campillo, M., Lacharmoise, P.D., Reparaz, J.S., Goni, A.R., Valiente, M., 2010. On the assessment of hydroxyapatite fluoridation by means of Raman scattering. J. Chem. Phys. 132, 244501.

Candeiro, C.R.A., Martinelli, A.G., 2006. A review of paleogeographical and chronostratigraphical distribution of mesoeucrocodylian species from the upper

Cretaceous beds from the Bauru (Brazil) and Neuquén (Argentina) groups, Southern South America. J. S. Am. Earth Sci. 22, 116–129.

Canfield, D.E., Raiswell, R., 1991. Pyrite formation and fossil preservation. In: Allison, P.A., Briggs, D.E.G. (Eds.), Taphonomy: Releasing the data locked in the fossil record. Plenum Press, New York, pp. 337–387.

Chen, H., Stimets, R.W., 2014. Fluorescence of trivalent neodymium in various materials excited by a 785 nm laser. Am. Mineral. 99, 332–342.

Chen, J., Huang, Y.W., Zhao, Y., 2014. Characterization of polycyclic aromatic hydrocarbons using Raman and surface-enhanced Raman spectroscopy. J. Raman Spectrosc. 46, 64–69.

Chen, J., Algeo, T. J., Zhao, L., Chen, Z. Q., Cao, L., Zhang, L., Li, Y., 2015. Diagenetic uptake of rare earth elements by bioapatite, with an example from Lower Triassic conodonts of South China. Earth-Sci. Rev. 149, 181–202.

Chen, W., Wang, Q., Meng, S., Yang, P., Jiang, L., Zou, X., Li, Z., Hu, S., 2017. Temperature-related changes of Ca and P release in synthesized hydroxylapatite, geological fluorapatite, and bone bioapatite. Chem. Geol. 451, 183–188.

Chinsamy-Turan, A., 2005. The Microstructure of Dinosaur Bone. Johns Hopkins University Press, Baltimore, p. 195.

Chukanov, N.V., Vigasina, M.F., 2020. Vibrational (Infrared and Raman) spectra of minerals and related compounds. Springer Mineralogy, Cham.

Clarke, J.B., Barker, M.J., 1993. Diagenesis in *Iguanodon* bones from the Wealden Group, Isle of Wight, southern England. Kaupia 2, 57–65.

Cloutis, E., Szymanski, P., Applin, D., Goltz, D., 2016. Identification and discrimination of polycyclic aromatic hydrocarbons using Raman spectroscopy. Icarus 274, 211–230.

Cowen, M. B., de Rafélis, M., Ségalen, L., Kear, B. P., Dumont, M., Žigaitė, Ž., 2025. Visualizing and quantifying biomineral preservation in fossil vertebrate dental remains. PeerJ 13, e18763.

Culka, A., Jehlička, J., 2018. Sequentially shifted excitation: A tool for suppression of laser-induced fluorescence in mineralogical applications using portable Raman spectrometers. J. Raman Spectrosc. 49, 526–537.

Cullen, T.M., Zhang, S., Spencer, J., Cousens, B., 2022. Sr-O-C isotope signatures reveal herbivore niche-partitioning in a Cretaceous ecosystem. Palaeontology 65, e12591.

Dal Sasso, G., Maritan, L., Usai, D., Angelini, I., Artioli, G., 2014. Bone diagenesis at the micro-scale: Bone alteration patterns during multiple burial phases at Al Khiday (Khartoum, Sudan) between the Early Holocene and the II century AD. Palaeogeogr. Palaeoclimatol. Palaeoecol. 416, 30–42.

Dal Sasso, G., Asscher, Y., Angelini, I., Nodari, L., Artioli, G., 2018a. A universal curve of apatite crystallinity for the assessment of bone integrity and preservation. Sci. Rep. 8, 1–13.

Dal Sasso, G., Angelini, I., Maritan, L., Artioli, G., 2018b. Raman hyperspectral imaging as an effective and highly informative tool to study the diagenetic alteration of fossil bones. Talanta 179, 167–176.

Darlim, G., Montefeltro, F. C., & Langer, M. C., 2021. 3D skull modelling and description of a new baurusuchid (Crocodyliformes, Mesoeucrocodylia) from the Late Cretaceous (Bauru Basin) of Brazil. J. Anat. 239, 622–662.

De Mul, F.F.M., Otto, C., Greve, J., Arends, J., Ten Bosch, J.J., 1988. Calculation of the Raman line broadening on carbonation in synthetic hydroxyapatite. J. Raman Spectrosc. 19, 13–21.

Delcourt, R., Brilhante, N.S., Pires-Domingues, R.A., Hendrickx, C., Grillo, O.N., Augusta, B.G., Maciel, B.S., Ghilardi, A.M., Ricardi-Branco, F., 2024. Biogeography of theropod dinosaurs during the Late Cretaceous: evidence from central South America. Zool. J. Linn. Soc., zlad184.

Domingo, L., Barroso-Barcenilla, F., Cambra-Moo, O., 2015. Seasonality and paleoecology of the Late Cretaceous multi-taxa vertebrate assemblage of “Lo Hueco” (central eastern Spain). Plos one 10, e0119968.

Durand, B., 1980. Kerogen, Insoluble Organic Matter from Sedimentary Rocks. Éditions Technip, Paris, p. 519.

Elliot, J.C., 2002. Calcium phosphate biominerals. Rev. Mineral. Geochem. 48, 427–453.

Farlow, J.O., Argast, A., 2006. Preservation of fossil bone from the Pipe Creek Sinkhole (Late Neogene, Grant County, Indiana U.S.A.). J. Geol. Soc. Korea 22, 51–75.

Fau, A., Beyssac, O., Gauthier, M., Panczer, G., Gasnault, O., Meslin, P.Y., Bernard, S., Maurice, S., Forni, O., Boulliard, J., Bosc, F., Drouet, C., 2022. Time-resolved Raman and luminescence spectroscopy of synthetic REE-doped hydroxylapatites and natural apatites. Am. Min. 107, 1341–1352.

Fernandes, L.A., Coimbra, A.M., 1996. A Bacia Bauru (Cretáceo Superior, Brasil). An. Acad. Bras. Ciênc. 68, 195–205.

Fernandes, L.A., Coimbra, A.M., 2000. Revisão estratigráfica da parte oriental da Bacia Bauru (Neocretáceo). Braz. J. Geol. 30, 717–728.

Fernandes, L.A., Ribeiro, C.M.M., 2015. Evolution and palaeoenvironment of the Bauru Basin (Upper Cretaceous, Brazil). J. S. Am. Earth Sci. 61, 71–90.

Freeman, J.J., Wang, A., Kuebler, K.E., Jolliff, B.L., Haskin, L.A., 2008. Characterization of natural feldspars by Raman spectroscopy for future planetary exploration. Canad. Mineral. 46, 1477–1500.

Fricke, H.C., Rogers, R.R., Eberth, D.A., Fiorillo, A.R., 2007. Stable isotope geochemistry of bonebed fossils: reconstructing paleoenvironments, paleoecology, and paleobiology. In: Rogers, R., Eberth, D., Fiorillo, A. (Eds.), Bonebeds: genesis, analysis, and paleobiological significance. University of Chicago Press, Chicago, pp. 437–490.

Gobbo, S.R., Bertini, R.J., 2023. Ostracoda non-marine biogeography in Campanian-Maastrichtian ages: South America, Africa and India connections. Rev. Micropaleontol. 79, 100716.

Godoy, P.L., Montefeltro, F.C., Norell, M.A., Langer, M.C., 2014. An additional baurusuchid from the Cretaceous of Brazil with evidence of interspecific predation among Crocodyliformes. PLoS One 9, e97138.

Goldberg, K., Garcia, A.J., 2000. Palaeobiogeography of the Bauru Group, a dinosaur-bearing Cretaceous unit, northeastern Paraná Basin, Brazil. Cretac. Res. 21, 241–254.

Gueriau, P., Mocuta, C., Bertrand, L., 2015. Cerium anomaly at microscale in fossils. Anal. Chem. 87, 8827–8836.

Halcrow, S.E., Rooney, J., Beavan, N., Gordon, K.C., Tayles, N., Gray, A., 2014. Assessing Raman spectroscopy as a prescreening tool for the selection of archaeological bone for stable isotopic analysis. PloS one 9, e98462.

Herwartz, D., Tütken, T., Jochum, K., Sander, P., 2013. Rare earth element systematics of fossil bone revealed by LA-ICPMS analysis. Geochim. Cosmochim. Acta 103, 161–183.

Holz, M., Schultz, C.L., 1998. Taphonomy of the south Brazilian Triassic herpetofauna: fossilization mode and implications for morphological studies. Lethaia 31, 335–345.

Huang, E., Chen, C.H., Huang, T., Lin, E. H., Xu, J.A., 2000. Raman spectroscopic characteristics of Mg-Fe-Ca pyroxenes. Am. Min. 85, 473–479.

Hubert, J.F., Panish, P.T., Chure, D.J., Prostak, K.S., 1996. Chemistry, microstructure, petrology, and diagenetic model of Jurassic dinosaur bones, Dinosaur National Monument, Utah. J. Sediment. Res. 66, 531–547.

Iori, F.V., Carvalho, I., 2018. The Cretaceous crocodyliform *Caipirasuchus*: behavioral feeding mechanisms. Cretac. Res. 84, 181–187.

Jurašeková, Z., Fabriciová, G., Silveira, L.F., Lee, Y.N., Gutak, J.M., Ataabadi, M.M., Kundrát, M., 2022. Raman spectra and ancient life: Vibrational ID profiles of fossilized (bone) tissues. Int. J. Mol. Sci. 23, 10689.

Kannan, S., Rocha, J.H.G., Agathopoulos, S., Ferreira, J.M.F., 2007. Fluorine-substituted hydroxyapatite scaffolds hydrothermally grown from aragonitic cuttlefish bones. Acta Biomater. 3, 243–249.

Keenan, S.W., 2016. From bone to fossil: A review of the diagenesis of bioapatite. Am. Mineral. 101, 1943–1951.

Keenan, S.W., 2023. Thermodynamic stabilities of apatite phases in a wetland system: Implications for bone diagenesis. Appl. Geochem. 148, 105546.

Keenan, S.W., Engel, A.S., 2017. Early diagenesis and recrystallization of bone. Geochim. Cosmochim. Acta 196, 209–223.

Kendall, C., Eriksen, A.M.H., Kontopoulos, I., Collins, M.J., Turner-Walker, G., 2018. Diagenesis of archaeological bone and tooth. Palaeogeogr. Palaeoclimatol. Palaeoecol. 491, 21–37.

Khalid, M., Bora, T., Ghaithi, A. A., Thukral, S., Dutta, J., 2018. Raman spectroscopy detects changes in bone mineral quality and collagen cross-linkage in staphylococcus infected human bone. Sci. Rep. 8, 9417.

King, C.L., Tayles, N., Gordon, K.C., 2011. Re-examining the chemical evaluation of diagenesis in human bone apatite. J. Archaeol. Sci. 38, 2222–2230.

Klock, C., Leuzinger, L., Santucci, R.M., Martinelli, A.G., Marconato, A., Marinho, T. S., Luz, Z., Vennemann, T., 2022. A bone to pick: Stable isotope compositions as tracers of food sources and paleoecology for notosuchians in the Brazilian Upper Cretaceous Bauru Group. Cretac. Res. 131, 105113.

Koch, P.L., 2007. Isotopic study of the biology of modern and fossil vertebrates. In: Michener, R., Lajtha, K. (Eds.), Stable Isotopes in Ecology and Environmental Science, Blackwell Publishing, 2, pp. 99–154.

Koenig, A.E., Rogers, R.R., Trueman, C.N., 2009. Visualizing fossilization using laser ablation–inductively coupled plasma–mass spectrometry maps of trace elements in Late Cretaceous bones. Geology 37, 511–514.

Koeppenkastrop, D., De Carlo, E.H., 1993. Uptake of rare earth elements from solution by metal oxides. Environ. Sci. Technol. 27, 1796–1802.

Kohn, M.J., 2008. Models of diffusion-limited uptake of trace elements in fossils and rates of fossilization. Geochimica et Cosmochimica Acta, 72(15), 3758–3770.

Kohn, M.J., Cerling, T.E., 2002. Stable isotope compositions of biological apatite. Rev. Mineral. Geochem. 48, 455–488.

Kohn, M.J., Moses, R.J., 2013. Trace element diffusivities in bone rule out simple diffusive uptake during fossilization but explain in vivo uptake and release. Proc. Natl. Acad. Sci. U.S.A. 110, 419–424.

Kohn, M.J., Schoeninger, M.J., Barker, W.W., 1999. Altered states: effects of diagenesis on fossil tooth chemistry. Geoch. Cosm. Act 63, 2737–2747.

Kolodny, Y., Luz, B., Sander, M., Clemens, W.A., 1996. Dinosaur bones: fossils or pseudomorphs? The pitfalls of physiology reconstruction from apatitic fossils. Palaeogeogr. Palaeoclimatol. Palaeoecol. 126, 161–171.

Korneisel, D.E., Nesbitt, S.J., Werning, S., Xiao, S., 2021. Putative fossil blood cells reinterpreted as diagenetic structures. PeerJ 9, e12651.

Kral, A. G., Lagos, M., Guagliardo, P., Tütken, T., Geisler, T., 2022. Rapid alteration of cortical bone in fresh-and seawater solutions visualized and quantified from the millimeter down to the atomic scale. Chem. Geol. 609, 121060.

Kral, A. G., Geisler, T., Wiedenbeck, M., Guagliardo, P., Tütken, T., 2024. Phosphate uptake is an essential process for rapid bone mineralization during early diagenesis–evidence from bone alteration experiments. Geochim. Cosmochim. Acta 375, 173–185.

Lafuente, B., Downs, R., Yang, H., Stone, N., 2015. The Power of Databases: The RRUFF Project. In: Armbruster, T., Danisi, R. (Eds.), Highlights in Mineralogical Crystallography. De Gruyter, Berlin, pp. 1–30.

Langer, M., Delcourt, R., Montefeltro, F., Silva-Júnior, J., Soler, M., Ferreira, G., Ruiz, J., Barcelos, L., Onary, S., Marsola, J., Castro, M., Cidade, G., Batezelli, A., 2022. The Bauru Basin in São Paulo and its tetrapods. Derbyana 43, e776.

Laker, R., 2024. Vertebrate fossil permineralization in a sequence stratigraphic context: Capsules of early diagenesis from shallow-marine siliciclastics (Eocene, Egypt). Palaios 39, 243–263.

Lécuyer, C., Bogey, C., Garcia, J.P., Grandjean, P., Barrat, J.A., Floquet, M., Bardet, N., Pereda-Superbiola, X., 2003. Stable isotope composition and rare earth element content of vertebrate remains from the Late Cretaceous of northern Spain (Laño): did the environmental record survive?. Palaeogeogr. Palaeoclimatol. Palaeoecol. 193, 457–471.

Lee-Thorp, J.A., Van der Merwe, N.J., 1991. Aspects of the chemistry of modern and fossil biological apatites. J. Archaeol. Sci. 18, 343–354.

LeGeros, R.Z., 1981. Apatites in biological systems. Prog. Cryst. Growth Charact. 4, 1–45.

Lim, D.I., Jung, H.S., Yang, S.Y., Yoo, H.S., 2004. Sequential growth of early diagenetic freshwater siderites in the Holocene coastal deposits, Korea. Sediment. Geol. 169, 107–120.

Lin, C.Y., Turchyn, A.V., Krylov, A., Antler, G., 2020. The microbially driven formation of siderite in salt marsh sediments. Geobiology 18, 207–224.

Loope, D.B., Kettler, R.M., Weber, K.A., Hinrichs, N.L., Burgess, D.T., 2012. Rinded iron-oxide concretions: hallmarks of altered siderite masses of both early and late diagenetic origin. Sedimentology 59, 1769–1781.

Luque, L., Alcalá, L., Mampel, L., Pesquero, M. D., Royo-Torres, R., Cobos, A., Espílez, E., González, A., Alloza, R., 2009. Mineralogical, elemental and chemical composition of dinosaur bones from Teruel (Spain). Journal of Taphonomy 7, 151–178.

Marchetti, I., Ricardi-Branco, F., Callefo, F., Delcourt, R., Galante, D., Jurigan, I., Carvalho, I., Tavares, S.A., 2019. Fossildiagenesis and ontogenetic insights of crocodyliform bones from the Adamantina Formation, Bauru Basin, Brazil. J. S. Am. Earth Sci. 96, 102327.

Marshall, A.O., Wehrbein, R.L., Lieberman, B.S., Marshall, C.P., 2012. Raman spectroscopic investigations of Burgess shale-type preservation: A new way forward. Palaios 27, 288–292.

Martin, J.E., Hassler, A., Montagnac, G., Therrien, F., Balter, V., 2022. The stability of dinosaur communities before the Cretaceous–Paleogene (K–Pg) boundary: A perspective from southern Alberta using calcium isotopes as a dietary proxy. Geol. Soc. Am. Bull. 134, 2548–2560.

Matsunaga, K., Murata, H., Shitara, K., 2010. Theoretical calculations of the thermodynamic stability of ionic substitutions in hydroxyapatite under an aqueous solution environment. J. Phys. Condens. Matter 22, 384210.

McLain, M., Ullmann, P., Ash, R., Bohnstedt, K., Nelsen, D., Clark, R., Brand, L., Chadwick, A., 2021. Independent confirmation of fluvial reworking at a Lance Formation (Maastrichtian) bonebed by traditional and chemical taphonomic analyses. Palaios 36, 193–215.

Melstrom, K.M., Irmis, R.B., 2019. Repeated evolution of herbivorous crocodyliforms during the age of dinosaurs. Curr. Biol. 29, 2389–2395.

Menegazzo, M.C., Catuneanu, O., Chang, H.K., 2016. The South American retroarc foreland system: the development of the Bauru Basin in the back-bulge province. Mar. Pet. Geol. 73, 131–156.

Meng, Q., Hooker, J., Cartwright, J., 2018. Displacive widening of calcite veins in shale: Insights into the force of crystallization. J. Sediment. Res. 88, 327–343.

Monger, H.C., Daugherty, L.A., Gile, L.H., 1991. A microscopic examination of pedogenic calcite in an Aridisol of southern New Mexico. In: Nettleton, W. (Ed.), Occurrence, characteristics, and genesis of carbonate, gypsum, and silica accumulations in soils, Special Publication Number 26, Madison, pp. 37–60.

Montefeltro, F. C., Larsson, H. C., Langer, M. C., 2011. A new baurusuchid (Crocodyliformes, Mesoeucrocodylia) from the Late Cretaceous of Brazil and the phylogeny of Baurusuchidae. PLoS One 6, e21916.

Montefeltro, F.C., Lautenschlager, S., Godoy, P.L., Ferreira, G.S., Butler, R.J., 2020. A unique predator in a unique ecosystem: modelling the apex predator within a Late Cretaceous crocodyliform-dominated fauna from Brazil. J. Anat. 237, 323–333.

Morris, M.D., Finney, W.F., 2004. Recent developments in Raman and infrared spectroscopy and imaging of bone tissue. Spectroscopy 18, 155–159.

Mortimer, R.J.G., Coleman, M.L., Rae, J.E., 1997. Effect of bacteria on the elemental composition of early diagenetic siderite: implications for palaeoenvironmental interpretations. Sedimentology 44, 759–765.

Nieto, M.N., Degrange, F.J., Sellers, K.C., Pol, D., Holliday, C.M., 2022. Biomechanical performance of the cranio-mandibular complex of the small notosuchian *Araripesuchus gomesii* (Notosuchia, Uruguaysuchidae). Anat. Rec. 305, 2695–2707.

Ősi, A., 2014. The evolution of jaw mechanism and dental function in heterodont crocodyliforms. Hist. Biol. 26, 279–414.

Owocki, K., Kremer, B., Wrzosek, B., Królikowska, A., Kaźmierczak, J., 2016. Fungal ferromanganese mineralisation in Cretaceous dinosaur bones from the Gobi Desert, Mongolia. PLoS One 11, e0146293.

Pan, Y., Fleet, M.E., 2002. Compositions of the apatite-group minerals: substitution mechanisms and controlling factors. Rev. Mineral. Geochem. 48, 13–49.

Pang, Y.X., Bao, X., 2003. Influence of temperature, ripening time and calcination on the morphology and crystallinity of hydroxyapatite nanoparticles. J. Eur. Ceram. Soc. 23, 1697–1704.

Penel, G., Delfosse, C., Descamps, M., Leroy, G., 2005. Composition of bone and apatitic biomaterials as revealed by intravital Raman microspectroscopy. Bone 36, 893–901.

Penel, G., Leroy, G., Bres, E., 1998. New preparation method of bone samples for Raman microspectrometry. Appl. Spectrosc. 52, 312–313.

Pereda-Suberbiola, X., Astibia, H., Murelaga, X., Elorza, J.J., Gómez-Alday, J.J., 2000. Taphonomy of the Late Cretaceous dinosaur-bearing beds of the Laño Quarry (Iberian Peninsula). Palaeogeogr. Palaeoclimatol. Palaeoecol. 157, 247–275.

Pérez, L.M., Otero, A., Muruaga, P.J.A., Gaetano, L.C., Leardi, J.M., Krapovickas, V., Poiré, D.G., 2022. Multiproxy taphonomic analysis in the Los Colorados Formation (Upper Triassic), Ischigualasto-Villa Unión Basin, Argentina: A case study through sauropodomorph remains. J. S. Am. Earth Sci. 118, 103925.

Pfretzschner, H.U., 2001a. Iron oxides in fossil bone. Neues Jahrb. Geol. Paläontol. 220, 417–429.

Pfretzschner, H.U., 2001b. Pyrite in fossil bone. Neues Jahrb. Geol. Paläontol. 220, 1–23.

Pfretzschner, H.U. (2004). Fossilization of Haversian bone in aquatic environments. Comptes Rendus Palevol. 3, 605–616.

Pfretzschner, H.U., Tütken, T., 2011. Rolling bones–Taphonomy of Jurassic dinosaur bones inferred from diagenetic microcracks and mineral infillings. Palaeogeogr. Palaeoclimatol. Palaeoecol. 310, 117–123.

Piga, G., Santos-Cubedo, A., Brunetti, A., Piccinini, M., Malgosa, A., Napolitano, E., Enzo, S., 2011. A multi-technique approach by XRD, XRF, FT-IR to characterize the diagenesis of dinosaur bones from Spain. Palaeogeogr. Palaeoclimatol. Palaeoecol. 310, 92–107.

Pinto, C.B., Lacerda, M.B., Rodrigues, B.L., Mussel, W., Romano, P.S.R., 2020. Geochemical characterization of fossil turtles from Tartaruguito outcrop (Upper Cretaceous, Bauru Basin, Presidente Prudente formation), São Paulo state, southeastern Brazil. J. S. Am. Earth Sci. 104, 102843.

Previtera, M.E., 2017. Bone microstructure and diagenesis of saurischian dinosaurs from the Upper Cretaceous (Neuquén Group), Argentina. Andean Geol. 44, 39–58.

Previtera, M.E., Mancuso, A.C., De la Fuente, Sánchez, E.S., 2016. Diagenetic analysis of tetrapod from the Upper Triassic, Puesto Viejo Group, Argentina. Andean Geol. 43, 197–214.

Rietveld, H.M., 1967. Line profiles of neutron powder-diffraction peaks for structure refinement. Acta Crystallogr., 22, 151–152.

Riff, D., Kellner, A.W.A., 2011. Baurusuchid crocodyliforms as theropod mimics: clues from the skull and appendicular morphology of *Stratiotosuchus maxhechti* (Upper Cretaceous of Brazil). Zool. J. Linn. Soc.163, S37–S56.

Riff, D. Souza, R.G., Cidade, G.M., Martinelli, A.G., Souza-Filho, J.P., 2012. Crocodilomorfos: A maior diversidade de répteis fósseis do Brasil. Terræ 9, 12–40.

Riga, B.J.G., Astini, R.A., 2007. Preservation of large titanosaur sauropods in overbank fluvial facies: a case study in the Cretaceous of Argentina. J. S. Am. Earth Sci. 23, 290–303.

Roberts, J.A., Kenward, P.A., Fowle, D.A., Goldstein, R.H., González, L.A., Moore, D.S., 2013. Surface chemistry allows for abiotic precipitation of dolomite at low temperature. Proc. Natl. Acad. Sci. U.S.A. 110, 14540–14545.

Rogers, R. R., Fricke, H. C., Addona, V., Canavan, R. R., Dwyer, C. N., Harwood, C. L., Koenig, A., Murray, R., Thole, J., Williams, J., 2010. Using laser ablation-inductively coupled plasma-mass spectrometry (LA-ICP-MS) to explore geochemical taphonomy of vertebrate fossils in the Upper Cretaceous Two Medicine and Judith River formations of Montana. Palaios 25, 183–195.

Rogers, R.R., Regan, A.K., Weaver, L.N., Thole, J.T., Fricke, H.C., 2020. Tracking authigenic mineral cements in fossil bones from the Upper Cretaceous (Campanian) Two Medicine and Judith River formations, Montana. Palaios 35, 135–150.

Sánchez-Pastor, N., Fesharaki, O., Hernando-Alonso, I., 2024. A multi-technique approach to characterize the composition and color of the fossil remains of the “Húmera Paleontological Site” from Spain. Episodes J. Int. Geosci. 47, 279–293.

Santelli, C.M., Webb, S.M., Dohnalkova, A.C., Hansel, C.M., 2011. Diversity of Mn oxides produced by Mn (II)-oxidizing fungi. Geoch. Cosm. Act 75, 2762–2776.

Schopf, J.W., Kudryavtsev, A.B., Agresti, D.G., Czaja, A.D., Wdowiak, T.J., 2005. Raman imagery: a new approach to assess the geochemical maturity and biogenicity of permineralized Precambrian fossils. Astrobiology 5, 333–371.

Schweitzer, M., Zheng, W., Cleland, T., Goodwin, M., Boatman, E., Theil, E., Marcus, M., Fakra, S., 2014. A role for iron and oxygen chemistry in preserving soft tissues, cells and molecules from deep time. Proc. R. Soc. B: Biol. Sci. 281, 20132741.

Senkayi, A.L., Dixon, J.B., Hossner, L.R., 1986. Todorokite, goethite, and hematite: alteration products of siderite in east Texas lignite overburden. Soil Science 142, 36–42.

Shah, F.A., 2020. Towards refining Raman spectroscopy-based assessment of bone composition. Sci. Rep. 10, 16662.

Shah, F., 2025. Revisiting the physical and chemical nature of the mineral component of bone. Acta Biomater. 196, 1–16.

Soares, P.C., Landim, P.M., Fulfaro, V.J., Sobreiro Neto, A.F., 1980. Ensaio de caracterizaç ao estratigráfica do Cretáceo no Estado de São Paulo: Grupo Bauru. Rev. Bras. Geociênc. 10, 177–185.

Soares, M.V.T., Basilici, G., Lorenzoni, P., Colombera, L., Mountney, N.P., Martinelli, A.G., Mesquita, A., Marinho, T., García, R., Marconato, A., 2020. Landscape and depositional controls on palaeosols of a distributive fluvial system (Upper Cretaceous, Brazil). Sediment. Geol. 410, 105774.

Sousa, D.V., Eltink, E., Oliveira, R.A.P., Félix, J.F., Guimarães, L.D.M., 2020. Diagenetic processes in Quaternary fossil bones from tropical limestone caves. Sci. Rep. 10, 1–16.

Sousa, D.V., Maia, P.V.S., Eltink, E., Guimarães, L., 2024. Biomolecules in Pleistocene fossils from tropical cave indicate fossil biofilm. Sci. Rep. 14, 21071.

Su, A., Bons, P.D., Chen, H., Feng, Y.X., Zhao, J.X., Song, J., 2022. Age, material source, and formation mechanism of bedding-parallel calcite beef veins: Case from the mature Eocene lacustrine shales in the Biyang Sag, Nanxiang Basin, China. GSA Bulletin 134, 1811–1833.

Suarez, C.A., Kohn, M.J., 2020. Caught in the act: A case study on microscopic scale physicochemical effects of fossilization on stable isotopic composition of bone. Geoch. Cosm. Act 268, 277–295.

Suarez, C.A., Morschhauser, E.M., Suarez, M.B., You, H., Li, D., Dodson, P., 2018. Rare earth element geochemistry of bone beds from the Lower Cretaceous Zhonggou Formation of Gansu Province, China. J. Vertebr. Paleontol. 38, 22–35.

Suarez, C.A., Macpherson, G.L., González, L.A., Grandstaff, D.E., 2010. Heterogeneous rare earth element (REE) patterns and concentrations in a fossil bone: implications for the use of REE in vertebrate taphonomy and fossilization history. Geoch. Cosm. Act 74, 2970–2988.

Takeuchi, A., Munar, M.L., Wakae, H., Maruta, M., Matsuya, S., Tsuru, K., Ishikawa, K., 2009. Effect of temperature on crystallinity of carbonate apatite foam prepared from α-tricalcium phosphate by hydrothermal treatment. Bio-Med. Mater. Eng. 19, 205-2011.

Thomas, D.B., Fordyce, R.E., Frew, R.D., Gordon, K.C., 2007. A rapid, non-destructive method of detecting diagenetic alteration in fossil bone using Raman spectroscopy. J. Raman Spectrosc. 38, 1533–1537.

Thomas, D.B., McGoverin, C.M., Fordyce, R.E., Frew, R.D., Gordon, K.C., 2011. Raman spectroscopy of fossil bioapatite—a proxy for diagenetic alteration of the oxygen isotope composition. Palaeogeogr. Palaeoclimatol. Palaeoecol. 310, 62–70.

Tomassini, R.L., Montalvo, C.I., Manera, T., Visconti, G., 2014. Mineralogy, Geochemistry and Paleohistology of Pliocene Mammals from the Monte Hermoso Formation (Argentina). Paedotherium bonaerense (Notoungulata, Hegetotheriidae) as a Case Study. Ameghiniana 51, 385–395.

Trueman, C.N., 1999. Rare earth element geochemistry and taphonomy of terrestrial vertebrate assemblages. Palaios 14, 555–568.

Trueman, C.N., Moore, A., 2007. Use of the stable isotope composition of fish scales for monitoring aquatic ecosystems. Terrestrial Ecology 1, 145–161.

Trueman, C.N., Tuross, N., 2002. Trace elements in recent and fossil bone apatite. Rev. Mineral. Geochem. 48, 489–521.

Trueman, C.N., Behrensmeyer, A.K., Potts, R., Tuross, N., 2006. High-resolution records of location and stratigraphic provenance from the rare earth element composition of fossil bones. Geoch. Cosm. Act 70, 4343–4355.

Trueman, C.N., Behrensmeyer, A.K., Tuross, N., Weiner, S., 2004. Mineralogical and compositional changes in bones exposed on soil surfaces in Amboseli National Park, Kenya: diagenetic mechanisms and the role of sediment pore fluids. J. Archaeol. Sci. 31, 721–739.

Trueman, C.N., Privat, K., Field, J., 2008. Why do crystallinity values fail to predict the extent of diagenetic alteration of bone mineral?. Palaeogeogr. Palaeoclimatol. Palaeoecol. 266, 160–167.

Trueman, C., Chenery, C., Eberth, D.A., Spiro, B., 2003. Diagenetic effects on the oxygen isotope composition of bones of dinosaurs and other vertebrates recovered from terrestrial and marine sediments. J. Geol. Soc. 160, 895–901.

Tütken, T., Vennemann, T.W., 2011. Fossil bones and teeth: preservation or alteration of biogenic compositions?. Palaeogeogr. Palaeoclimatol. Palaeoecol. 310, 1–8.

Tütken, T., Vennemann, T.W., Pfretzschner, H.U., 2011. Nd and Sr isotope compositions in modern and fossil bones–Proxies for vertebrate provenance and taphonomy. Geoch. Cosm. Act 75, 5951–5970.

Ullmann, P.V., Voegele, K.K., Grandstaff, D.E., Ash, R.D., Zheng, W., Schroeter, E. R., Schweitzer, M., Lacovara, K.J., 2020. Molecular tests support the viability of rare earth elements as proxies for fossil biomolecule preservation. Sci. Rep. 10, 1–11.

Ullmann, P., Caputo, C., Snyder, K., Chadwick, A., Ash, R., 2025. Trace element taphonomy of the Hanson Ranch Edmontosaurus bonebed supports its origin via transportation of a mass death assemblage. Chem. Geol. 672, 122501.

Vietti, L.A., Bailey, J.V., Fox, D.L., Rogers, R.R., 2015. Rapid formation of framboidal sulfides on bone surfaces from a simulated marine carcass fall. Palaios 30, 327–334.

Wang, J., Hao, X., Kundrát, M., Liu, Z., Uesugi, K., Jurašeková, Z., Guo, B., Hoshino, M., Li, Y., Monfroy, Q., Zhou, B., Fabriciová, G., Kang, A., Wang, M., Si, Y., Gao, J., Xu, G., Li, Z., 2020. Bone tissue histology of the Early Cretaceous bird *Yanornis*: evidence for a diphyletic origin of modern avian growth strategies within Ornithuromorpha. Hist. Biol. 32, 1422–1434.

Watts, N.L., 1978. Displacive calcite: evidence from recent and ancient calcretes. Geology 6, 699–703.

Weiner, S., Price, P.A., 1986. Disaggregation of bone into crystals. Calcified Tissue International 39, 365–375.

White, M.A., Bell, P.R., Campione, N.E., Sansalone, G., Brougham, T., Bevitt, J.J., Molnar, R., Cook, A., Wroe, S., Elliott, D.A., 2022. Abdominal contents reveal Cretaceous crocodyliforms ate dinosaurs. Gondwana Res. 106, 281–302.

Wiemann, J., Fabbri, M., Yang, T.R., Stein, K., Sander, P.M., Norell, M.A., Briggs, D.E., 2018. Fossilization transforms vertebrate hard tissue proteins into N-heterocyclic polymers. Nat. Commun. 9, 4741.

Wings, O., 2004. Authigenic minerals in fossil bones from the Mesozoic of England: poor correlation with depositional environments. Palaeogeogr. Palaeoclimatol. Palaeoecol. 204, 15–32.

Wopenka, B., Pasteris, J.D., 1993. Structural characterization of kerogens to granulite-facies graphite: applicability of Raman microprobe spectroscopy. Am. Min. 78, 533–557.

Wopenka, B., Pasteris, J.D., 2005. A mineralogical perspective on the apatite in bone. Mater. Sci. Eng. C 25, 131–143.

Wright, V.P., Tucker, E., 1991. Calcretes. Blackwell, Oxford, p. 352.

Yamamura, D., 2024. Investigating the Timing of Carbonate Precipitations and Their Potential Impact on Fossil Preservation in the Hell Creek Formation. Minerals 14, 1133.

Yang, Q., Wang, Y.L., 2007. Raman spectra of fossil dinosaurs from different regions. Guang Pu Xue Yu Guang Pu Fen Xi 27, 2468–2471.

Zhang, L., Cao, L., Zhao, L., Algeo, T. J., Chen, Z. Q., Li, Z., Lv, Z., Wang, X., 2017. Raman spectral, elemental, crystallinity, and oxygen-isotope variations in conodont apatite during diagenesis. Geoch. Cosm. Act 210, 184–207.

Zhao, Y., Wei, W., Li, S., Yang, T., Zhang, R., Somerville, I., Santosh, M., Wei, H., Wu, J., Yang, J., Chen, W., Tang, Z., 2021. Rare earth element geochemistry of carbonates as a proxy for deep-time environmental reconstruction. Palaeogeogr. Palaeoclimatol. Palaeoecol. 574, 110443.

Figure Captions

Figure 1. Geological map of the Bauru Basin in the states of São Paulo and Minas Gerais, showing the localities where the specimens analyzed in this study were collected. 1, Furnas Farm, Jales; 2, General Salgado; 3, Km-34, Auriflama; 4, Ibirá; 5, Inhaúmas-Arantes Farm, Gurinhatã; 6, Marília. Modified from Fernandes and Coimbra (2000) and Menegazzo et al. (2016).

Figure 2. XRF results (log10-transformed counts) of selected elements in fossil, rock, and modern samples. Modern and fossil samples include bone, enamel, and dentine. A synthetic bone standard (std) was also analyzed for comparison.

Figure 3. Representative BSE/SEM image and EDS elemental maps obtained from a transverse polished section of a rib (LPRP/USP 0697). Elemental maps show the widespread presence of Ca, P, and O in the bone sample, which reflects the composition of fluorapatite. Some voids are filled by Mn, Ce, and Fe-bearing minerals and calcite.

Figure 4. SEM-BSE images and EDS elemental maps show bone breakage and displacement, presumably caused by calcite growth. A. Osteoderm from LPRP/USP 0786. B. Osteoderm from LPRP/USP 0791. C. Vertebra from LPRP/USP 0050.

Figure 5. Raman spectra from a modern crocodylian and fossil crocodyliforms showing the main inorganic and organic bands in the 200–1800 cm^{-1} (A) and 2500–3400 cm^{-1} (B) ranges. Spectra are vertically offset for clarity. Raman bands are indicated with asterisks; red asterisks denote peaks in fossil skeletal elements that occur within organic band locations.

Figure 6. Relationship between width (FWHM) and position of the $\nu_1(PO_4)$ band for different apatite samples. The grey area corresponds to an alteration field defined by

Thomas et al. (2011), where diagenetic modification probably changed original isotopic compositions. FWHM = Full Width at Half Maximum height. FAp = Fluorapatite.

Figure 7. Raman spectra exhibiting bands of still unknown origin (marked with asterisks) in *P. sera* fossil bone (LPRP/USP 0050) and fossil dentine from an unidentified crocodyliform (LPRP/USP 0794). G-band and D-band of graphite (from the RRUFF database), the organic bands of a modern crocodylian bone, and the fluorescence bands of a mineral apatite (see Culka and Jehlička, 2018) are also shown in the figure.

Figure 8. Simplified overview of diagenetic processes involved in the preservation of the studied crocodyliforms at the micro- and nanoscale. A. The organic components of bone in living individuals include cells, a fibrous proteinaceous matrix, and a network of blood vessels and nervous fibers. B. After death, the decomposition of the organic matter creates voids within the bone tissue. C. Infiltration of fluids with mobile ions leads to the precipitation of oxides (Fe-, Mn-, and possibly Ce-bearing minerals) and carbonates (calcite and siderite) inside empty cavities. D. At the microscale, bioapatite is interwoven with organic matter. E. The degradation of protective organics opens pore spaces and exposes the bioapatite crystals to diagenetic fluids. F. Substitutions occur at every site of the bioapatite unit cell (Ca^{2+}, PO_4^{3-}, OH^-). Particularly important is the substitution of F^- at the OH^- site, which contracts the unit cell and favors the precipitation of new apatite phases with larger crystal sizes, ultimately reducing bone porosity. Images in A, B, and C were partially drawn based on an image from Servier Medical Art. D was redrawn and modified from Keenan (2016). The crystal structure in E was redrawn and modified from Matsunaga et al. (2010).

Table 1. Summary of the samples analyzed in this study. Abbreviations: XRF, energy-dispersive X-ray fluorescence; SEM-EDS, scanning electron microscopy coupled with energy-dispersive X-ray spectroscopy; MRS, micro-Raman spectroscopy; XRD, X-ray diffraction.

Specimen	Taxon	Locality	Sample	Methods
LPRP/USP 0697	*Aphaurosuchus escharafacies*	Furnas Farm, Jales	Osteoderm 1	SEM-EDS; XRF; XRD; MRS
LPRP/USP 0697	*Aphaurosuchus escharafacies*	Furnas Farm, Jales	Osteoderm 2	SEM-EDS
LPRP/USP 0697	*Aphaurosuchus escharafacies*	Furnas Farm, Jales	Rib	SEM-EDS
LPRP/USP 0697	*Aphaurosuchus escharafacies*	Furnas Farm, Jales	Tooth	SEM-EDS
LPRP/USP 0697	*Aphaurosuchus escharafacies*	Furnas Farm, Jales	Sediment	SEM-EDS; XRF; XRD; MRS
LPRP/USP 0229a	*Aplestosuchus sordidus*	Buriti Farm, General Salgado	Osteoderm 1	SEM-EDS; XRF; XRD; MRS
LPRP/USP 0229a	*Aplestosuchus sordidus*	Buriti Farm, General Salgado	Osteoderm 2	SEM-EDS
LPRP/USP 0229a	*Aplestosuchus sordidus*	Buriti Farm, General Salgado	Rib	SEM-EDS
LPRP/USP 0229a	*Aplestosuchus sordidus*	Buriti Farm, General Salgado	Sediment	XRF; XRD; MRS
LPRP/USP 0786	Baurusuchidae	Buriti Farm, General Salgado	Osteoderm	SEM-EDS; XRF; XRD; MRS
LPRP/USP 0786	Baurusuchidae	Buriti Farm, General Salgado	Long bone 1	SEM-EDS
LPRP/USP 0786	Baurusuchidae	Buriti Farm, General Salgado	Long bone 2	SEM-EDS
LPRP/USP 0786	Baurusuchidae	Buriti Farm, General Salgado	Weathered bone	SEM-EDS
LPRP/USP 0786	Baurusuchidae	Buriti Farm, General Salgado	Sediment	SEM-EDS; XRF; XRD; MRS
LPRP/USP 0791	Baurusuchidae	General Salgado	Osteoderm	SEM-EDS
LPRP/USP 0642	Crocodyliformes	General Salgado	Osteoderm	SEM-EDS
LPRP/USP 0794	Crocodyliformes	Auriflama region	Tooth	SEM-EDS; XRF; XRD; MRS
LPRP/USP 0794	Crocodyliformes	Auriflama region	Sediment	XRF; XRD; MRS
MPPC SN	Crocodyliformes	Ibirá region	Tooth 1	SEM-EDS; XRF; XRD
MPPC SN	Crocodyliformes	Ibirá region	Tooth 2	SEM-EDS; XRF
LPRP/USP 0049A	*Pissarrachampsa sera*	Inhaúmas-Arantes Farm, Gurinhatã	Rib	SEM-EDS; MRS
LPRP/USP 0049A	*Pissarrachampsa sera*	Inhaúmas-Arantes Farm, Gurinhatã	Osteoderm	SEM-EDS
LPRP/USP 0049A	*Pissarrachampsa sera*	Inhaúmas-Arantes Farm, Gurinhatã	Sediment	SEM-EDS
LPRP/USP 0049B	*Pissarrachampsa sera*	Inhaúmas-Arantes Farm, Gurinhatã	Long bone 1	SEM-EDS
LPRP/USP 0049B	*Pissarrachampsa sera*	Inhaúmas-Arantes Farm, Gurinhatã	Long bone 2	SEM-EDS
LPRP/USP 0049B	*Pissarrachampsa sera*	Inhaúmas-Arantes Farm, Gurinhatã	Sediment	SEM-EDS
LPRP/USP 0050	*Pissarrachampsa sera*	Inhaúmas-Arantes Farm, Gurinhatã	Vertebra	SEM-EDS; XRF; XRD; MRS
LPRP/USP 0050	*Pissarrachampsa sera*	Inhaúmas-Arantes Farm, Gurinhatã	Sediment	SEM-EDS; XRF; XRD; MRS
LPRP/USP 0740 (ex L0065)	*Pissarrachampsa sera*	Inhaúmas-Arantes Farm, Gurinhatã	Phalanx	SEM-EDS

LPRP/USP SN	*Mariliasuchus* sp.	Marília region	Osteoderm	SEM-EDS; XRF; XRD; MRS
LPRP/USP SN	*Mariliasuchus* sp.	Marília region	Femur	SEM-EDS
LPRP/USP SN	*Mariliasuchus* sp.	Marília region	Sediment	SEM-EDS; XRF; XRD; MRS

Table 2. Raman band assignments for skeletal tissues, host rock matrix and infill material.

Material Type	Assignment	Raman shift/ cm^{-1}	References
Skeletal Tissue	$\nu_2(PO_4)$	~430	Penel et al. (1998); Morris and Finney (2004)
	$\nu_4(PO_4)$	~584	Penel et al. (1998); Morris and Finney (2004)
	Proline	851–857	Morris ad Finney (2004); Alebrahim et al. (2014), Khalid et al. (2018), Bērziņš et al. (2019)
	$\nu_1(PO_4)$	959–962	Penel et al. (1998); Morris ad Finney (2004); Bērziņš et al. (2019); Shah (2020)
	Phenylalanine	~1003	Penel et al. (2005)
	$\nu_1(CO_3)$ B-type	1070-1072	Penel et al. (1998); Morris and Finney (2004); Shah (2020)
	Amide III	1230–1250	Penel et al. (1998); Wiemann et al. (2018)
	C-H bending	1447–1452	Penel et al. (1998); Morris and Finney (2004)
	Amide I	1650–1690	Penel et al. (1998); Wiemann et al. (2018)
	C-H stretching	2800-3060	Penel et al. (1998); Halcrow et al. (2014)
Matrix and Infill	Hematite	227, 293, 411, 497, 612	Chukanov and Vigasina (2020)
	Quartz	263, 354, 463	Chukanov and Vigasina (2020)
	K-feldspar	282, 475, 513	Freeman et al. (2008)
	Calcite	283, 713, 1086	Chukanov and Vigasina (2020)
	Plagioclase	480, 509	Freeman et al. (2008)
	Pyroxene (Diopside-hedenbergite series)	665, 1011	Huang et al. (2000)

Figure 8. Simplified overview of diagenetic processes involved in the preservation of the studied crocodyliforms at the micro- and nanoscale. A. The organic components of bone in living individuals include cells, a fibrous proteinaceous matrix, and a network of blood vessels and nervous fibers. B. After death, the decomposition of the organic matter creates voids within the bone tissue. C. Infiltration of fluids with mobile ions leads to the precipitation of oxides (Fe-, Mn-, and possibly Ce-bearing minerals) and carbonates (calcite and siderite) inside empty cavities. D. At the microscale, bioapatite is interwoven with organic matter. E. The degradation of protective organics opens pore spaces and exposes the bioapatite crystals to diagenetic fluids. F. Substitutions occur at every site of the bioapatite unit cell (Ca^{2+}, PO_4^{3-}, OH^-). Particularly important is the substitution of F^- at the OH^- site, which contracts the unit cell and favors the precipitation of new apatite phases with larger crystal sizes, ultimately reducing bone porosity. Images in A, B, and C were partially drawn based on an image from Servier Medical Art. D was redrawn and modified from Keenan (2016). The crystal structure in E was redrawn and modified from Matsunaga et al. (2010).

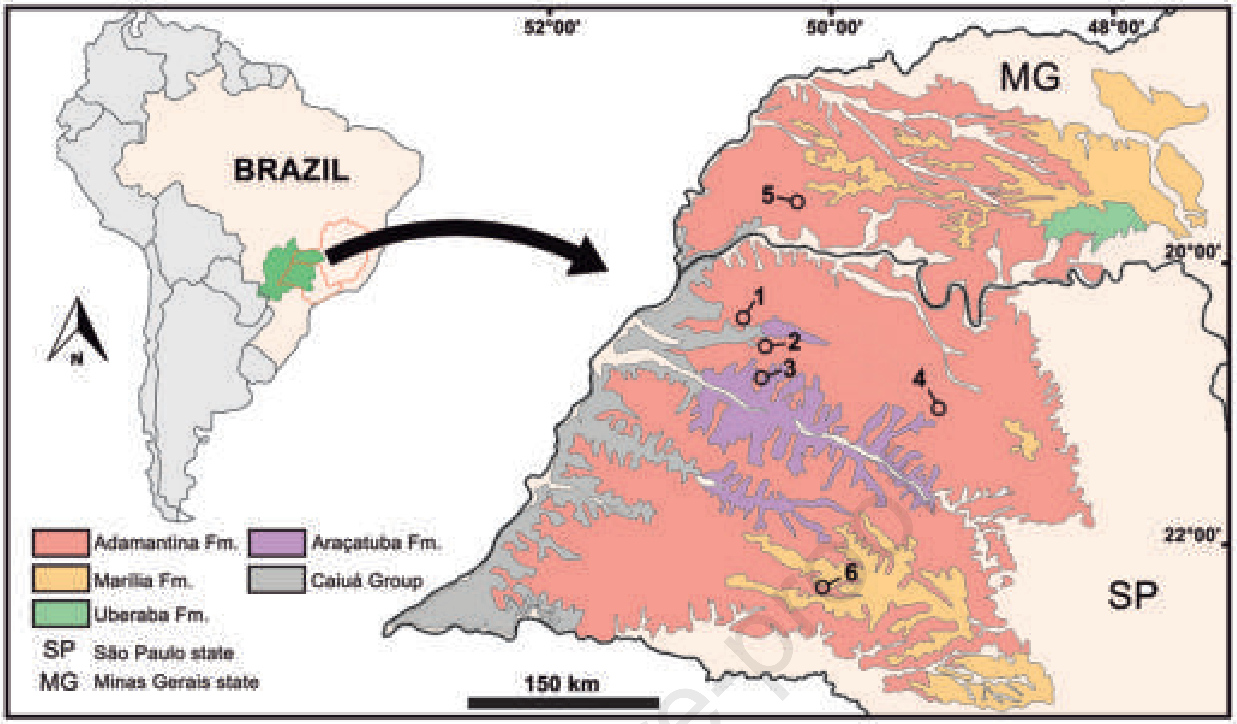
52°00'
50°00'
48°00'
20°00'
22°00'
BRAZIL
MG
SP
N
1
2
3
4
5
6
150 km
Adamantina Fm.
Araçatuba Fm.
Marilia Fm.
Caiuá Group
Uberaba Fm.
SP São Paulo state
MG Minas Gerais state

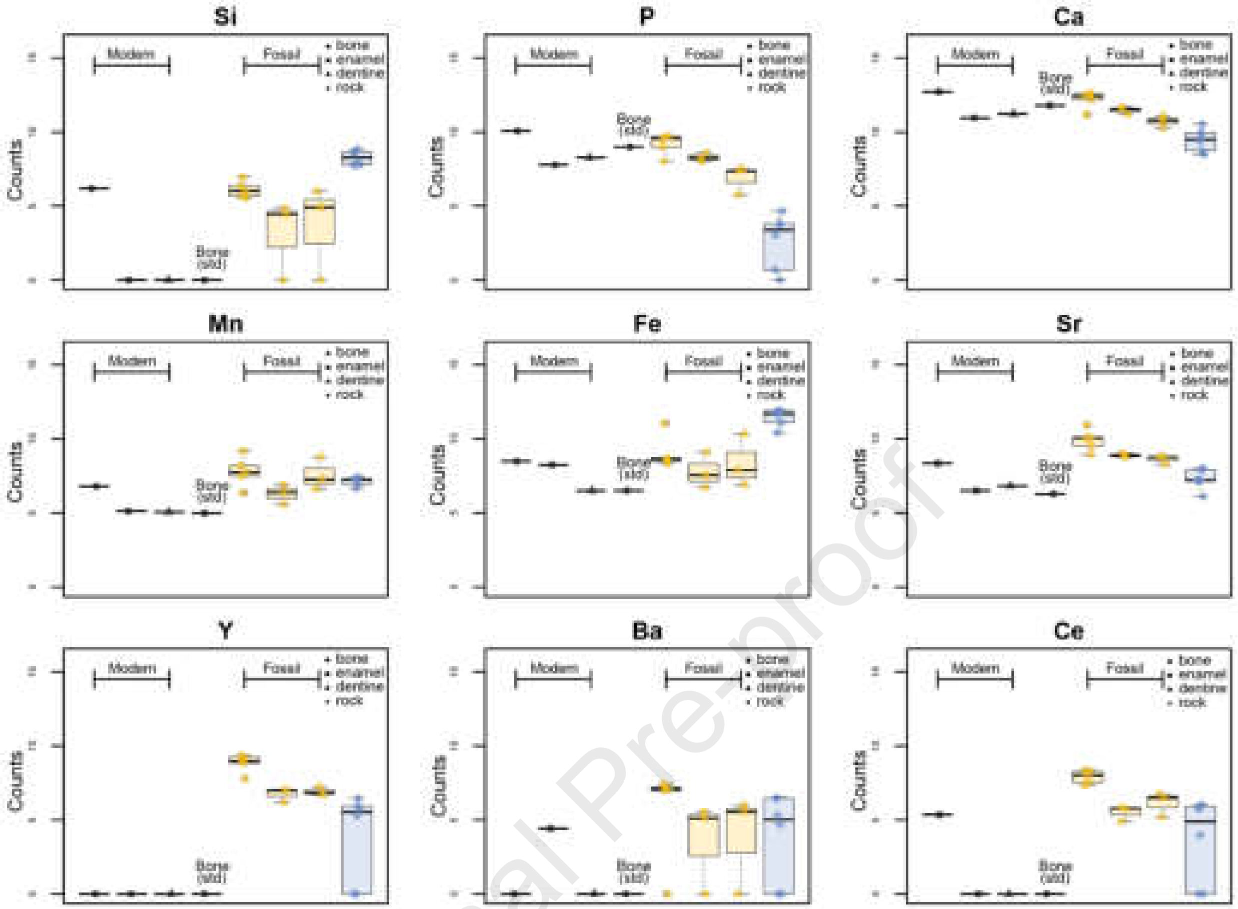
Si
P
Ca
Mn
Fe
Sr
Y
Ba
Ce
Counts
Modern
Fossil
Bone (std)
bone
enamel
dentine
rock

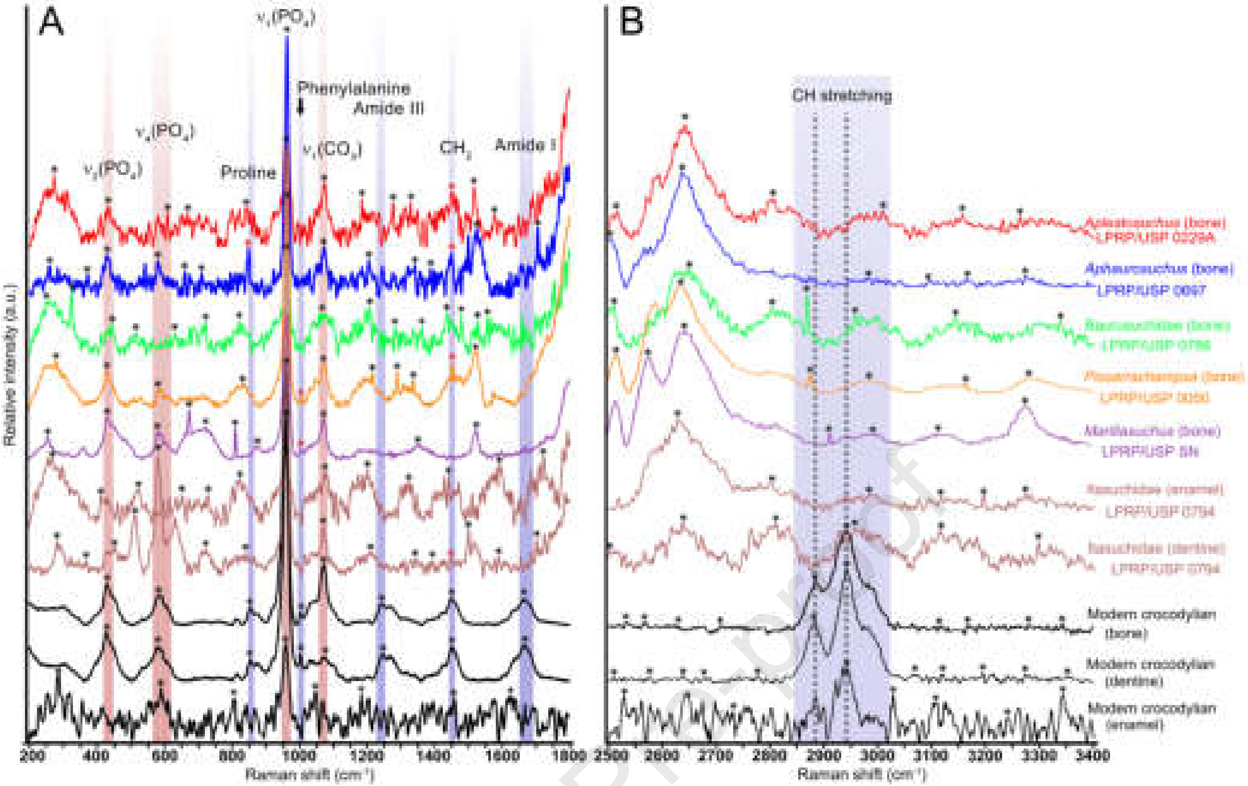
A
ν1(PO4)
Phenylalanine
Amide III
ν4(PO4)
ν2(PO4)
Proline
ν1(CO3)
CH2
Amide I
Relative intensity (a.u.)
200
400
600
800
1000
1200
1400
1600
1800
Raman shift (cm-1)
B
CH stretching
Aplestosuchus (bone)
LPRP/USP 0229A
Aphaurosuchus (bone)
LPRP/USP 0697
Baurusuchidae (bone)
LPRP/USP 0786
Pissarrachampsa (bone)
LPRP/USP 0050
Mariliasuchus (bone)
LPRP/USP SN
Itasuchidae (enamel)
LPRP/USP 0794
Itasuchidae (dentine)
LPRP/USP 0794
Modern crocodylian
(bone)
Modern crocodylian
(dentine)
Modern crocodylian
(enamel)
2500
2600
2700
2800
2900
3000
3100
3200
3300
3400
Raman shift (cm-1)

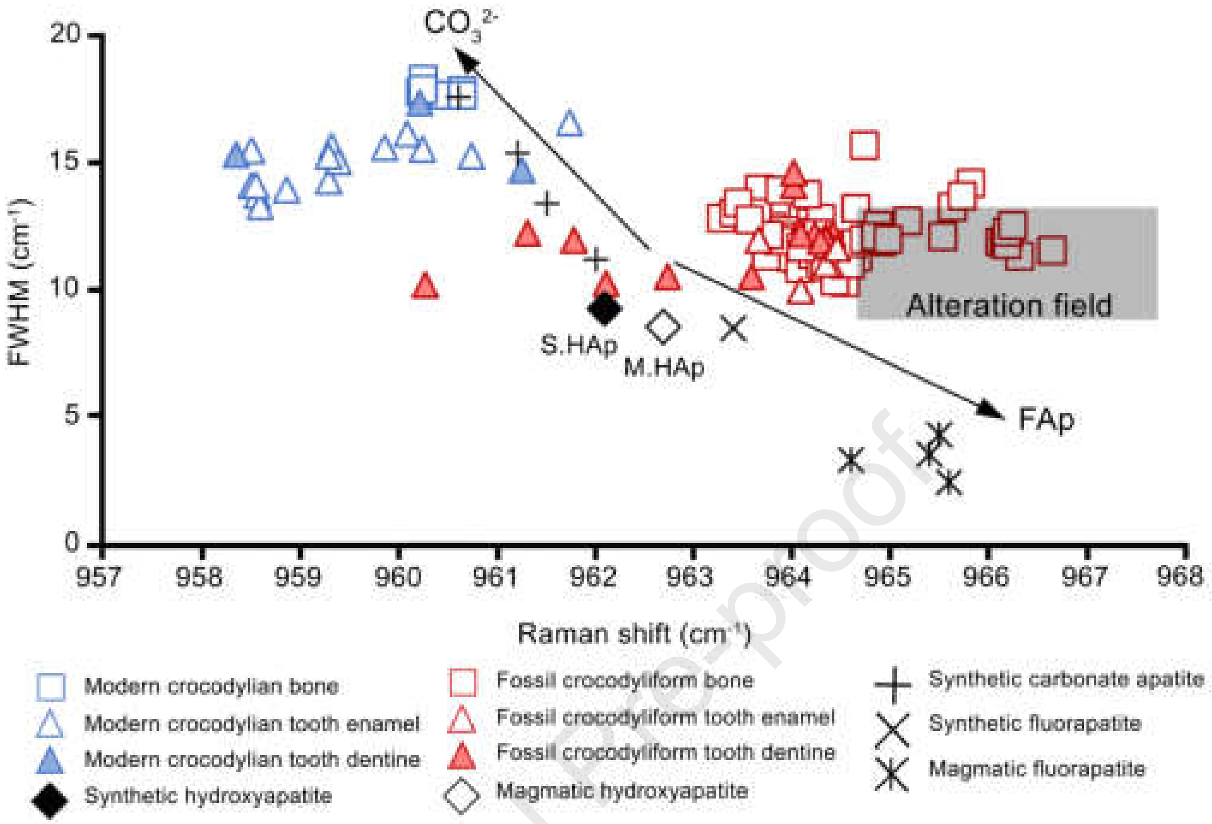

CO_3^{2-}
FAp
Alteration field
S.HAp
M.HAp
FWHM (cm⁻¹)
Raman shift (cm⁻¹)
0
5
10
15
20
957
958
959
960
961
962
963
964
965
966
967
968
Modern crocodylian bone
Modern crocodylian tooth enamel
Modern crocodylian tooth dentine
Synthetic hydroxyapatite
Fossil crocodyliform bone
Fossil crocodyliform tooth enamel
Fossil crocodyliform tooth dentine
Magmatic hydroxyapatite
Synthetic carbonate apatite
Synthetic fluorapatite
Magmatic fluorapatite

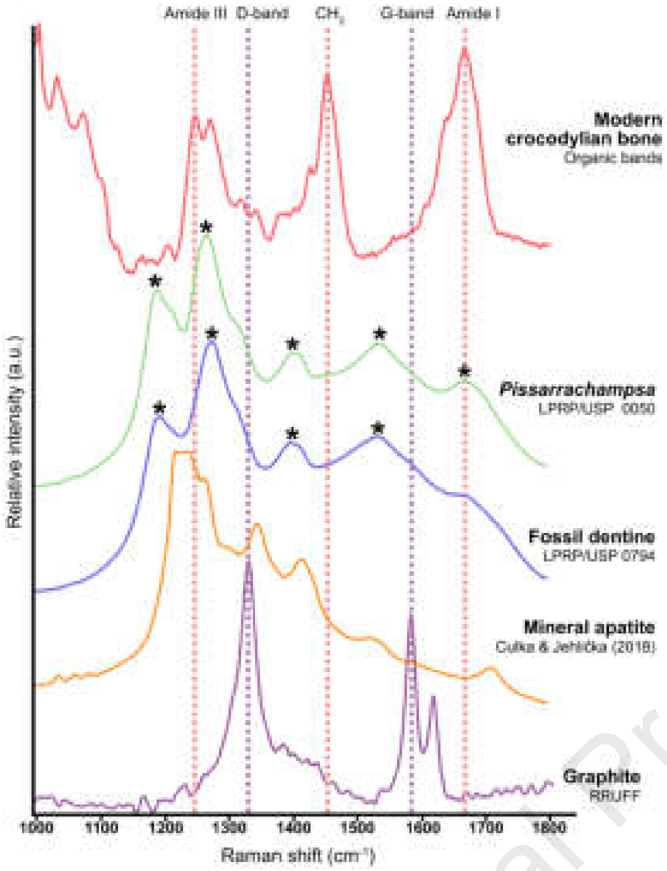
Amide III
D-band
CH_2
G-band
Amide I
Modern crocodylian bone
Organic bands
Pissarrachampsa
LPRP/USP 0050
Fossil dentine
LPRP/USP 0794
Mineral apatite
Culka & Jehlička (2018)
Graphite
RRUFF
Relative intensity (a.u.)
Raman shift (cm^{-1})
1000
1100
1200
1300
1400
1500
1600
1700
1800

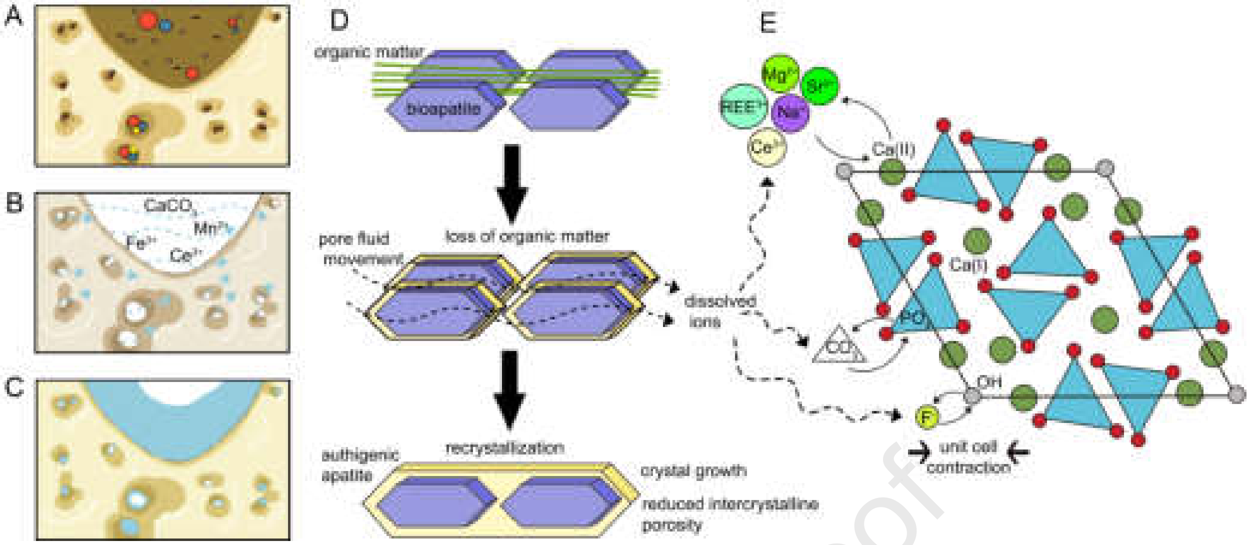
A
B
$CaCO_3$
Mn^{2+}
Fe^{3+}
Ce^{3+}
C
D
organic matter
bioapatite
pore fluid movement
loss of organic matter
dissolved ions
recrystallization
authigenic apatite
crystal growth
reduced intercrystalline porosity
E
Mg^{2+}
Sr^{2+}
REE^{3+}
Na^{+}
Ce^{3+}
Ca(II)
Ca(I)
PO_4
CO_3
OH
F^-
unit cell contraction

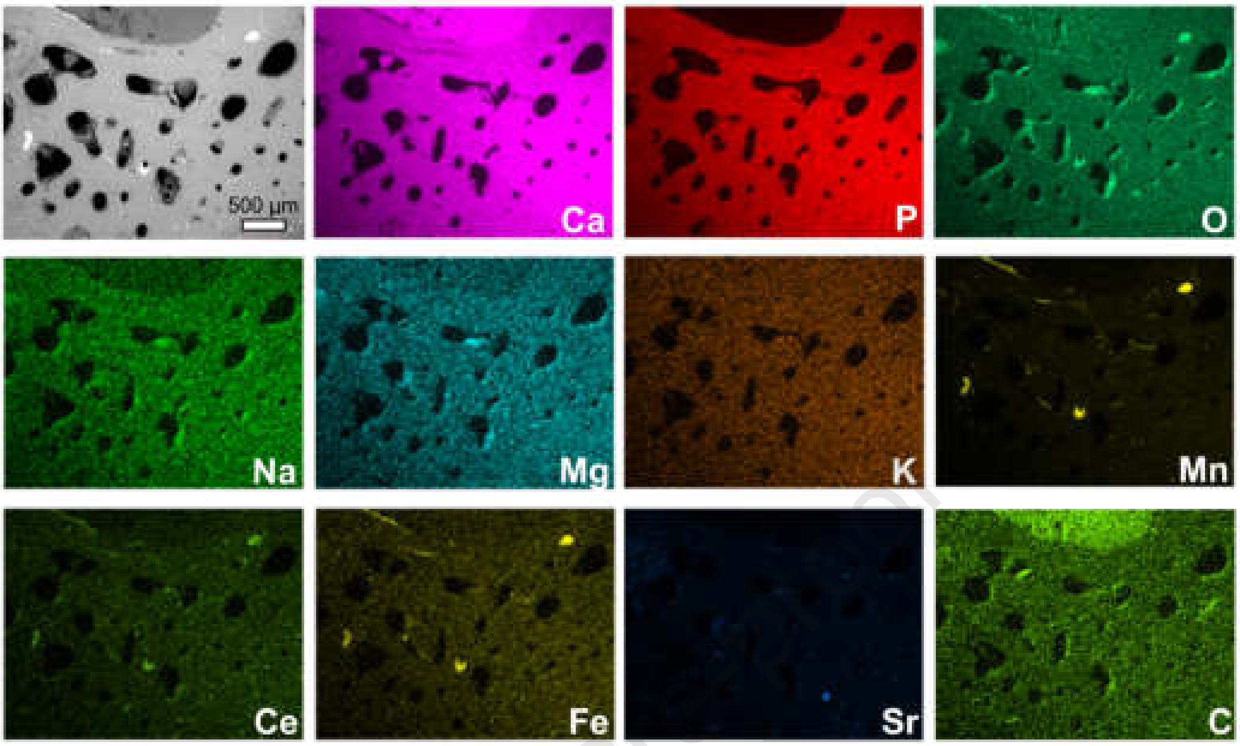
500 µm
Ca
P
O
Na
Mg
K
Mn
Ce
Fe
Sr
C

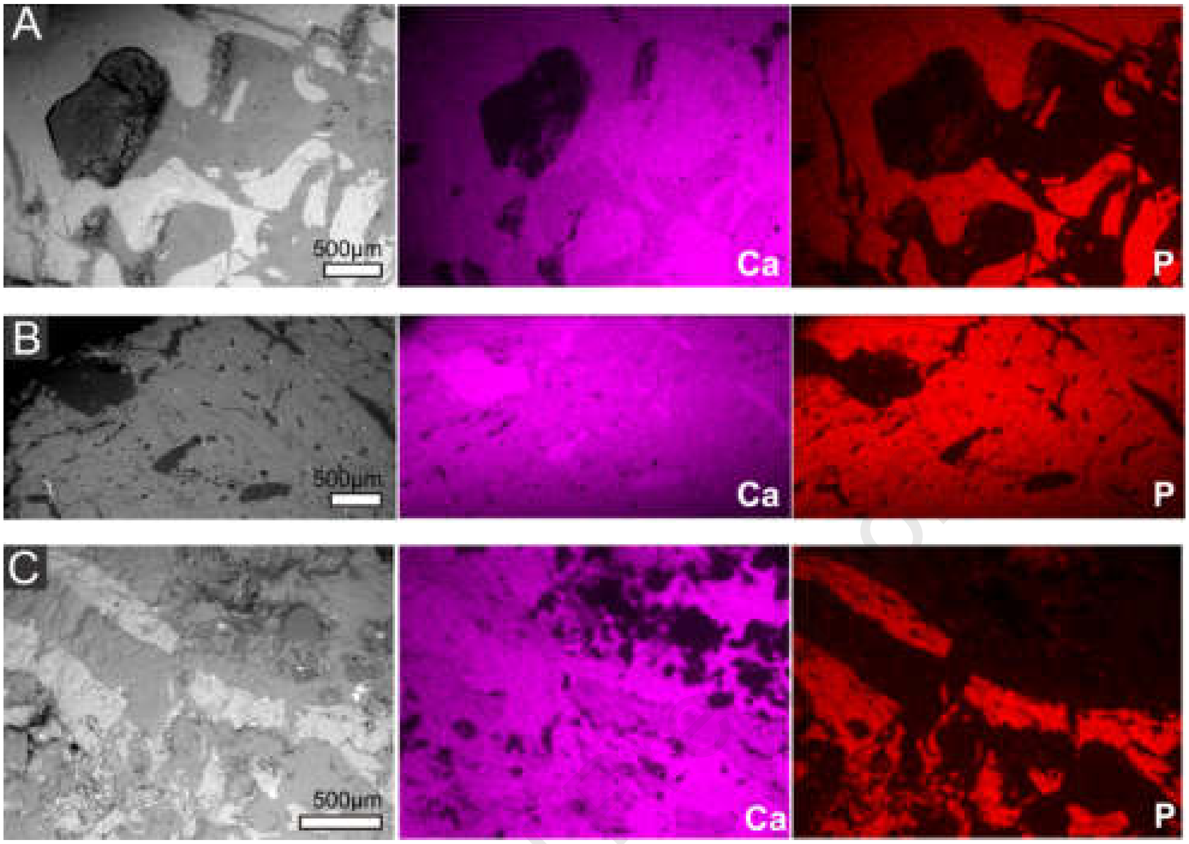
A
500µm
Ca
P
B
500µm
Ca
P
C
500µm
Ca
P